

**XENONnT analysis: Signal reconstruction, calibration, and event selection**

E. Aprile<sup>1</sup>, J. Aalbers<sup>2</sup>, K. Abe<sup>3</sup>, S. Ahmed Maouloud<sup>4</sup>, L. Althueser<sup>5</sup>, B. Andrieu<sup>4</sup>, E. Angelino<sup>6,7</sup>, J. R. Angevaere<sup>8</sup>, D. Antón Martín<sup>9</sup>, F. Arneodo<sup>10</sup>, L. Baudis<sup>11</sup>, M. Bazyk<sup>12</sup>, L. Bellagamba<sup>13</sup>, R. Biondi<sup>14</sup>, A. Bismark<sup>11</sup>, K. Boese<sup>14</sup>, A. Brown<sup>15</sup>, G. Bruno<sup>12</sup>, R. Budnik<sup>16</sup>, J. M. R. Cardoso<sup>17</sup>, A. P. Cimental Chávez<sup>11</sup>, A. P. Colijn<sup>8</sup>, J. Conrad<sup>18</sup>, J. J. Cuenca-García<sup>11</sup>, V. D'Andrea<sup>7,\*</sup>, L. C. Daniel Garcia<sup>4</sup>, M. P. Decowski<sup>8</sup>, A. Deisting<sup>19</sup>, C. Di Donato<sup>20</sup>, P. Di Gangi<sup>13</sup>, S. Diglio<sup>12</sup>, K. Eitel<sup>21</sup>, A. Elykov<sup>21</sup>, A. D. Ferella<sup>20,7</sup>, C. Ferrari<sup>7</sup>, H. Fischer<sup>15</sup>, T. Flehmke<sup>18</sup>, M. Flierman<sup>8</sup>, W. Fulgione<sup>6,7</sup>, C. Fuselli<sup>8</sup>, P. Gaemers<sup>8</sup>, R. Gaior<sup>4</sup>, M. Galloway<sup>11</sup>, F. Gao<sup>22</sup>, S. Ghosh<sup>23</sup>, R. Giacomobono<sup>24</sup>, R. Glade-Beucke<sup>15</sup>, L. Grandi<sup>9</sup>, J. Grigat<sup>15</sup>, H. Guan<sup>23</sup>, M. Guida<sup>14</sup>, P. Gyorgy<sup>19</sup>, R. Hamann<sup>14</sup>, A. Higuera<sup>25</sup>, C. Hils<sup>19</sup>, L. Hoetzsch<sup>14</sup>, N. F. Hood<sup>26</sup>, M. Iacovacci<sup>24</sup>, Y. Itow<sup>27</sup>, J. Jakob<sup>5</sup>, F. Joerg<sup>14</sup>, Y. Kaminaga<sup>3</sup>, M. Kara<sup>21</sup>, P. Kavargin<sup>16</sup>, S. Kazama<sup>27</sup>, M. Kobayashi<sup>27</sup>, D. Koke<sup>5</sup>, A. Kopec<sup>26,†</sup>, F. Kuger<sup>15</sup>, H. Landsman<sup>16</sup>, R. F. Lang<sup>23</sup>, L. Levinson<sup>16</sup>, I. Li<sup>25</sup>, S. Li<sup>28</sup>, S. Liang<sup>25</sup>, Y.-T. Lin<sup>14</sup>, S. Lindemann<sup>15</sup>, M. Lindner<sup>14</sup>, K. Liu<sup>22</sup>, J. Loizeau<sup>12</sup>, F. Lombardi<sup>19</sup>, J. Long<sup>9,‡</sup>, J. A. M. Lopes<sup>17,§</sup>, T. Luce<sup>15</sup>, Y. Ma<sup>26</sup>, C. Macolino<sup>20,7</sup>, J. Mahlstedt<sup>18</sup>, A. Mancuso<sup>13</sup>, L. Manenti<sup>10</sup>, F. Marignetti<sup>24</sup>, T. Marrodán Undagoitia<sup>14</sup>, K. Martens<sup>3</sup>, J. Masbou<sup>12</sup>, E. Masson<sup>4</sup>, S. Mastroianni<sup>24</sup>, A. Melchiorre<sup>20</sup>, J. Merz<sup>19</sup>, M. Messina<sup>7</sup>, A. Michael<sup>5</sup>, K. Miuchi<sup>29</sup>, A. Molinaro<sup>6</sup>, S. Moriyama<sup>3</sup>, K. Morā<sup>1</sup>, Y. Mosbacher<sup>16</sup>, M. Murra<sup>1</sup>, J. Müller<sup>15</sup>, K. Ni<sup>26</sup>, U. Oberlack<sup>19</sup>, B. Paetsch<sup>19</sup>, Y. Pan<sup>4</sup>, Q. Pellegrini<sup>4</sup>, R. Peres<sup>11</sup>, C. Peters<sup>25</sup>, J. Pienaar<sup>9,16</sup>, M. Pierre<sup>8,||</sup>, G. Plante<sup>1</sup>, T. R. Pollmann<sup>8</sup>, L. Principe<sup>12</sup>, J. Qi<sup>26</sup>, J. Qin<sup>25</sup>, D. Ramírez García<sup>11</sup>, M. Rajado<sup>11</sup>, R. Singh<sup>23</sup>, L. Sanchez<sup>25</sup>, J. M. F. dos Santos<sup>17</sup>, I. Sarnoff<sup>10</sup>, G. Sartorelli<sup>13</sup>, J. Schreiner<sup>14</sup>, D. Schulte<sup>5</sup>, P. Schulte<sup>5</sup>, H. Schulze Eiβing<sup>5</sup>, M. Schumann<sup>15</sup>, L. Scotto Lavina<sup>4</sup>, M. Selvi<sup>13</sup>, F. Semeria<sup>13</sup>, P. Shagin<sup>19</sup>, S. Shi<sup>1</sup>, J. Shi<sup>22</sup>, M. Silva<sup>17</sup>, H. Simgen<sup>14</sup>, A. Takeda<sup>3</sup>, P.-L. Tan<sup>18</sup>, A. Terliuk<sup>14,¶</sup>, D. Thers<sup>12</sup>, F. Toschi<sup>21</sup>, G. Trincherio<sup>6</sup>, C. D. Tunnell<sup>25</sup>, F. Tönnies<sup>15</sup>, K. Valerius<sup>21</sup>, S. Vecchi<sup>30</sup>, S. Vetter<sup>21</sup>, F. I. Villazon Solar<sup>19</sup>, G. Volta<sup>14,\*\*</sup>, C. Weinheimer<sup>5</sup>, M. Weiss<sup>16</sup>, D. Wenz<sup>5</sup>, C. Wittweg<sup>11</sup>, V. H. S. Wu<sup>21</sup>, Y. Xing<sup>12</sup>, D. Xu<sup>1</sup>, Z. Xu<sup>1</sup>, M. Yamashita<sup>3</sup>, L. Yang<sup>26</sup>, J. Ye<sup>31</sup>, L. Yuan<sup>9</sup>, G. Zavattini<sup>30</sup>, and M. Zhong<sup>26</sup>

(XENON Collaboration)<sup>††</sup><sup>1</sup>Physics Department, Columbia University, New York, New York 10027, USA<sup>2</sup>Nikhef and the University of Groningen, Van Swinderen Institute, 9747AG Groningen, Netherlands<sup>3</sup>Kamioka Observatory, Institute for Cosmic Ray Research, and Kavli Institute for the Physics and Mathematics of the Universe (WPI), University of Tokyo, Higashi-Mozumi, Kamioka, Hida, Gifu 506-1205, Japan<sup>4</sup>LPNHE, Sorbonne Université, CNRS/IN2P3, 75005 Paris, France<sup>5</sup>Institut für Kernphysik, Westfälische Wilhelms-Universität Münster, 48149 Münster, Germany<sup>6</sup>INAF-Astrophysical Observatory of Torino, Department of Physics, University of Torino and INFN-Torino, 10125 Torino, Italy<sup>7</sup>INFN-Laboratori Nazionali del Gran Sasso and Gran Sasso Science Institute, 67100 L'Aquila, Italy<sup>8</sup>Nikhef and the University of Amsterdam, Science Park, 1098XG Amsterdam, Netherlands<sup>9</sup>Department of Physics and Kavli Institute for Cosmological Physics, University of Chicago, Chicago, Illinois 60637, USA<sup>10</sup>New York University Abu Dhabi - Center for Astro, Particle and Planetary Physics, Abu Dhabi, United Arab Emirates<sup>11</sup>Physik-Institut, University of Zürich, 8057 Zürich, Switzerland<sup>12</sup>SUBATECH, IMT Atlantique, CNRS/IN2P3, Université de Nantes, Nantes 44307, France<sup>13</sup>Department of Physics and Astronomy, University of Bologna and INFN-Bologna, 40126 Bologna, Italy<sup>14</sup>Max-Planck-Institut für Kernphysik, 69117 Heidelberg, Germany<sup>15</sup>Physikalisches Institut, Universität Freiburg, 79104 Freiburg, Germany<sup>16</sup>Department of Particle Physics and Astrophysics, Weizmann Institute of Science, Rehovot 7610001, Israel<sup>17</sup>LIBPhys, Department of Physics, University of Coimbra, 3004-516 Coimbra, Portugal<sup>18</sup>Oskar Klein Centre, Department of Physics, Stockholm University, AlbaNova, Stockholm SE-10691, Sweden<sup>19</sup>Institut für Physik and Exzellenzcluster PRISMA+, Johannes Gutenberg-Universität Mainz, 55099 Mainz, Germany

<sup>20</sup>*Department of Physics and Chemistry, University of L'Aquila, 67100 L'Aquila, Italy*<sup>21</sup>*Institute for Astroparticle Physics, Karlsruhe Institute of Technology, 76021 Karlsruhe, Germany*<sup>22</sup>*Department of Physics and Center for High Energy Physics, Tsinghua University, Beijing 100084, People's Republic of China*<sup>23</sup>*Department of Physics and Astronomy, Purdue University, West Lafayette, Indiana 47907, USA*<sup>24</sup>*Department of Physics "Ettore Pancini," University of Napoli and INFN-Napoli, 80126 Napoli, Italy*<sup>25</sup>*Department of Physics and Astronomy, Rice University, Houston, Texas 77005, USA*<sup>26</sup>*Department of Physics, University of California San Diego, La Jolla, California 92093, USA*<sup>27</sup>*Kobayashi-Maskawa Institute for the Origin of Particles and the Universe, and Institute for Space-Earth Environmental Research, Nagoya University, Furo-cho, Chikusa-ku, Nagoya, Aichi 464-8602, Japan*<sup>28</sup>*Department of Physics, School of Science, Westlake University, Hangzhou 310030, People's Republic of China*<sup>29</sup>*Department of Physics, Kobe University, Kobe, Hyogo 657-8501, Japan*<sup>30</sup>*INFN-Ferrara and Dipartimento di Fisica e Scienze della Terra, Università di Ferrara, 44122 Ferrara, Italy*<sup>31</sup>*School of Science and Engineering, The Chinese University of Hong Kong, Shenzhen, Guangdong, 518172, People's Republic of China*

(Received 18 September 2024; accepted 28 January 2025; published 24 March 2025)

The XENONnT experiment, located at the INFN Laboratori Nazionali del Gran Sasso, Italy, features a 5.9 tonne liquid xenon time projection chamber surrounded by an instrumented neutron veto, all of which is housed within a muon veto water tank. Because of extensive shielding and advanced purification to mitigate natural radioactivity, an exceptionally low background level of  $(15.8 \pm 1.3)$  events/(tonne · year · keV) in the (1,30) keV region is reached in the inner part of the time projection chamber. XENONnT is, thus, sensitive to a wide range of rare phenomena related to dark matter and neutrino interactions, both within and beyond the Standard Model of particle physics, with a focus on the direct detection of dark matter in the form of weakly interacting massive particles. From May 2021 to December 2021, XENONnT accumulated data in rare-event search mode with a total exposure of one tonne · year. This paper provides a detailed description of the signal reconstruction methods, event selection procedure, and detector response calibration, as well as an overview of the detector performance in this time frame. This work establishes the foundational framework for the “blind analysis” methodology we are using when reporting XENONnT physics results.

DOI: [10.1103/PhysRevD.111.062006](https://doi.org/10.1103/PhysRevD.111.062006)

## I. INTRODUCTION

A wide range of astrophysical and cosmological observations indicate a Universe where only a small portion of the matter is baryonic and the total mass content is dominated by a new, yet unknown, form of nonluminous

substance, or dark matter [1]. Several candidate particles, not contained in the Standard Model of particle physics, can solve the dark matter problem, and one of the most intriguing are the weakly interacting massive particles (WIMPs) [2]. In recent years, axions [3] and bosonic dark matter [4], such as dark photons, have gathered a lot of attention in the scientific community. Nevertheless, WIMPs are still one of the main search candidates in the quest to identify dark matter. In the context of direct detection of dark matter, dual-phase xenon time projection chambers (TPCs) are at the forefront of probing WIMPs in the GeV–TeV mass range [5–7], with the XENON project being a key contributor to this effort.

Together with Ref. [8], this paper reports on the analysis methods employed for the main physics analyses of the first science run of XENONnT (SR0) [5,9], focusing on the techniques of signal reconstruction, event selection, and detector calibration.

The XENONnT experiment is the present stage of the XENON project. Most of the service systems and infrastructure have been inherited from its predecessor, the

\* Also at INFN-Roma Tre, 00146 Roma, Italy.

† Present address: Department of Physics and Astronomy, Bucknell University, Lewisburg, PA, USA.

‡ Contact author: [jylong@uchicago.edu](mailto:jylong@uchicago.edu)

§ Also at Coimbra Polytechnic—ISEC, 3030-199 Coimbra, Portugal.

|| Contact author: [maxime.pierre@nikhef.nl](mailto:maxime.pierre@nikhef.nl)

¶ Also at Physikalisches Institut, Universität Heidelberg, Heidelberg, Germany.

\*\* Contact author: [giovanni.volta@mpi-hd.mpg.de](mailto:giovanni.volta@mpi-hd.mpg.de)†† Contact author: [xenon@lngs.infn.it](mailto:xenon@lngs.infn.it)

Published by the American Physical Society under the terms of the [Creative Commons Attribution 4.0 International license](https://creativecommons.org/licenses/by/4.0/). Further distribution of this work must maintain attribution to the author(s) and the published article's title, journal citation, and DOI. Funded by SCOAP<sup>3</sup>.

XENON1T experiment [10]. The XENONnT experiment is located in Hall B of the INFN Laboratori Nazionali del Gran Sasso, Italy, consisting of three nested detectors. A water tank with 10 m diameter and height functions as a Cherenkov muon veto. Next to the water tank, a three-floor service building hosts the experiment's infrastructure. Within the water tank, a neutron veto (NV) [11] is installed, which consists of an inner region enclosed by reflective panels, equipped with 120 Hamamatsu R5912-100-10 8" photomultiplier tubes (PMTs). The TPC is placed at the center of the water tank inside a double-walled stainless-steel cryostat. Twenty-four polytetrafluoroethylene (PTFE) reflector panels surround the TPC volume, marking the boundary of the TPC active volume with a 1.34 m diameter which is filled with 5.9 tonnes of liquid xenon (LXe), in a double-walled vacuum-insulated cryostat. Two arrays of 3" Hamamatsu R11410-21 PMTs [12], totaling 494 units, are placed at the top and the bottom of the cylinder.

An electric drift field is generated in the LXe by a cathode placed 60 mm above the bottom PMT array and a gate electrode at the top. These two electrodes, separated by 1486 mm at LXe temperature, demarcate the active region. The detector is filled with LXe to 5.0 mm above the gate electrode, above which xenon exists in gaseous form. An anode electrode is placed 8 mm above the gate to establish an extraction field across the liquid-gas interface. Two screening electrodes at 5.3 mm above the bottom and 40.7 mm below the top PMTs protect the photosensors from the electric fields. Two and four additional wires, for the gate and the anode, respectively, are installed perpendicular to the other wires to minimize the effect of gravitational and electrostatic sagging. These wires are referenced as the perpendicular wires and create localized variations in signal properties. Two concentric sets of oxygen-free copper field-shaping rings ensure the uniformity of the drift field and minimize charge-insensitive regions. Both inner and outer cryostats have domed upper sections with several access ports connecting the TPC to the rest of the infrastructure. Additional information can be found in Refs. [13,14].

Like other noble liquids, xenon responds to energy depositions in the form of atom recoils, resulting in atom ionizations and excitations. Excited xenon atoms combine to form excited dimers whose dissociations emit 175 nm scintillation photons [15] which are measured by the PMTs and are referred to as the S1 signal. The free electrons produced in the ionization channel are displaced from the interaction site by the electric drift field toward the liquid-gas interface at the top of the TPC. At this interface, the much stronger extraction field extracts the electrons into the gas phase and creates the proportional scintillation S2 signal [16]. The partial recombination of free electrons with ions also forms excited dimers, whose dissociation contributes to the S1 signal. The splitting of energy between ionizations and excitations results in an anticorrelation between the S1

and S2 signals. The S2/S1 signal ratio enables the differentiation between electronic recoils (ER) and nuclear recoils (NR). NR events, which include expected signals from WIMPs [5], coherent elastic neutrino-nucleus scattering [17], and neutrons as a source of background, are of primary interest. Conversely, ER events, caused by  $\beta$  particles, gamma radiation, and neutrino-electron scattering, constitute the predominant background in the search for WIMPs. However, ER events can also be used to probe new physics, such as axions [9], and double weak decay searches [18].

The XENONnT experiment was installed in 2020 and commissioned by spring 2021. The first scientific data-acquisition periods, referred to as SR0, is detailed in Sec. II. Section III describes the data processor used to convert the raw data obtained during this period into physical quantities and properties of S1 and S2 signals and the event simulation framework used to evaluate the performance of the data processor. The processor also reconstructs the interaction position of each event (Sec. IV) and applies corrections to the measured signals to account for spatial and temporal dependencies (Sec. V). The leading ER and NR searches are based on selecting a clean sample of single-scatter events (Sec. VI) inside a central fiducial volume with a reduced background level. Finally, the energy reconstruction performance is presented in Sec. VII.

## II. DETECTOR OPERATION AND STABILITY

### A. First science run

The datasets recorded during SR0 between July 6 and November 10, 2021 include physics data, with a total live time of 97.1 days and used for rare-event-search analyses [5,9], as well as calibration data performed before, during,

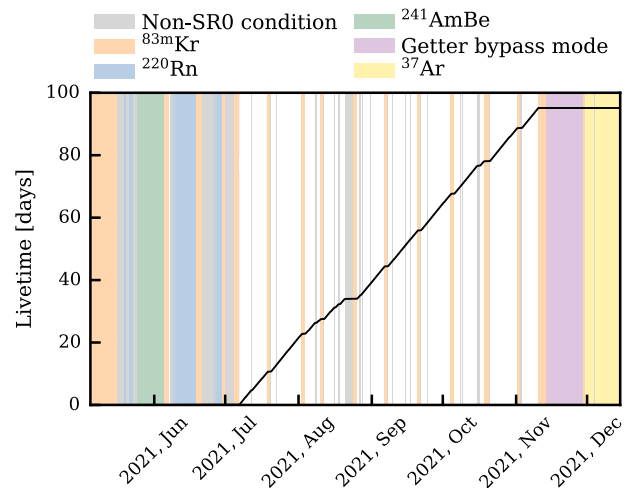


FIG. 1. Live time development of XENONnT SR0. The solid black line shows the cumulative science data without dead time correction. Colored bands highlight calibration periods and intervals of detector conditions unsuitable for scientific analysis from PMT trips, hot-spot periods, and maintenance operations.

and after this period [13]. The SR0 data-taking campaign is shown in Fig. 1. The following types of calibration sources are used to quantify the detector response to ionizing radiation:  $^{83\text{m}}\text{Kr}$ ,  $^{241}\text{AmBe}$ ,  $^{220}\text{Rn}$ , and  $^{37}\text{Ar}$ .

$^{83\text{m}}\text{Kr}$  atoms were injected through the gas xenon recirculation path into the LXe TPC volume about every two weeks.  $^{83\text{m}}\text{Kr}$  decays via subsequent emission of 32.1 and 9.4 keV conversion electrons, with half-lives of 1.83 h and 157 ns, respectively [19]. The first decay is slow enough that the source distributes uniformly in the detector after injection, as shown by the distribution of the reconstructed positions of  $^{83\text{m}}\text{Kr}$ . The fast decay coincidence provides a signature of two sequential S1 signals, reconstructed as either a merged S1 peak (41.5 keV) or two separate S1 peaks (32.1 and 9.4 keV). Most of the S2 signals are not separable because S2's have  $\mathcal{O}(1)$   $\mu\text{s}$  widths.  $^{83\text{m}}\text{Kr}$  events were used to monitor and characterize spatial and temporal variations of detector response at those energies.

An  $^{241}\text{AmBe}$  source, inserted in the water tank and deployed in different positions around the outer cryostat, was used to characterize the TPC response to NR events and evaluate the neutron veto detection efficiency.

Two calibration sources,  $^{220}\text{Rn}$  and  $^{37}\text{Ar}$  [20], were used to characterize the ER response. The first provided a continuous ER spectrum at low energies thanks to its  $\beta$  emitter daughter  $^{212}\text{Pb}$  [21], and it was used for ER band modeling and to develop data-selection criteria. The decay of  $^{37}\text{Ar}$ , with a 35 days half-life, leads to low-energy events at 2.82 and 0.27 keV via (K- and L-shell) electron capture [22]. These were primarily used to further understand the detector response near the energy threshold. To avoid unwanted  $^{37}\text{Ar}$  contamination in the physics search data, the source was injected at the end of the SR0 and removed afterward via cryogenic distillation [23].

Besides the physics search and detector calibrations, the detector was operated in different conditions; e.g., PMTs gain calibration and anode-ramped down periods due to strong single-electron emission. These periods are excluded from SR0 and marked gray in Fig. 1.

To investigate the XENON1T low-energy ER excess [24], a test was conducted by modifying the xenon recirculation scheme to potentially enhance tritium sources. It is speculated that tritium could account for the observed ER excess. Thus, the adjustment involved bypassing a GXe getter upstream of the radon removal system [13], thereby potentially increasing the concentration of water, tritiated water, and tritiated hydrogen within the xenon target. As a result, this specific data-acquisition mode, referred to as getter bypass mode, aimed to understand the potential impact of tritium contamination. However, the test results indicated no significant increase in tritium level.

## B. Detector conditions

During the commissioning phase of the detector, the field strengths within the different TPC regions were optimized

to achieve the best possible detection efficiency and ER/NR discrimination. However, following a cathode short-circuit event, the cathode and bottom screening electrodes were shorted. As a result, the drift field in the active volume had to be reduced to  $22.9^{+0.5}_{-0.3}$  V/cm (uncertainties reflect the standard deviation across the volume), with cathode, gate, and anode at  $-2.75$  kV, 300 V, and 4.9 kV, respectively. The reduced drift field resulted in a long maximum electron drift time of 2.2 ms. Furthermore, sporadic and localized high rates of single-electron events (hot spots) limited the extraction field intensity to 2.9 kV/cm. The mitigation of these hot spots required a few temporary shutdowns of the top electrode stack and, consequently, an interruption of the data acquisition. The voltage steps between successive field-shaping electrodes were optimized by setting the independent power supply of the top field-shaping wire electrode to  $+0.65$  kV to reduce field inhomogeneity and the charge-insensitive mass inside the TPC volume [14].

During the entire science run, the detector was operated under stable thermodynamic conditions with average detector pressure, liquid xenon temperature, and liquid-gas interface level (from the gate) of  $(1.890 \pm 0.004)$  bar,  $(-97.15 \pm 0.4)$  °C, and  $(5.0 \pm 0.2)$  mm, respectively.

The cryogenic distillation campaigns, conducted during the detector commissioning for krypton and continuously during SR0 for radon, reduced the  $^{\text{nat}}\text{Kr}/\text{Xe}$  molar concentration to  $(56 \pm 36)$  ppq and the  $^{222}\text{Rn}$  level to  $(1.87 \pm 0.09)$   $\mu\text{Bq}/\text{kg}$  [25]. Similarly, evacuating the detector for a period of 3 months following the cryostats' sealing helped to reduce the water content by minimizing outgassing. The water concentration of the vaporized liquid xenon circulating from the cryostat measured during SR0 was consistently below the sensor sensitivity of 0.5 ppb (mol/mol). Finally, the upgraded gas and new liquid xenon purification lines lowered the concentration of electronegative impurities, e.g.,  $\text{O}_2$ , to a level such that electron lifetimes<sup>1</sup> consistently exceeded  $\sim 10$  ms during SR0.

The voltages supplied to the photosensors were individually optimized during the commissioning phase to minimize the afterpulses rate as well as spurious light emissions while keeping a uniform single-photoelectron (PE) acceptance at the digitizer threshold (typically, 15 analog-to-digital converter (ADC) counts) equal to  $(91.2 \pm 0.2)\%$ . This configuration was achieved with an average PMT gain equal to  $(1.87 \pm 0.35) \times 10^6$ , where the reported uncertainty reflects the standard deviation over all PMTs, and a maximum bias voltage limited to  $-1.5$  kV. The PMT gains were determined at least once a week by flashing LEDs [13] and using the analysis method from XENON1T [26]. Figure 2 illustrates the gain trends during SR0 of five stable PMTs (numbered 0, 100, 256, 332, and

<sup>1</sup>Defined as the mean survival time for a free electron in the detector before it is attached to an impurity. See Sec. VB 1 for additional information.

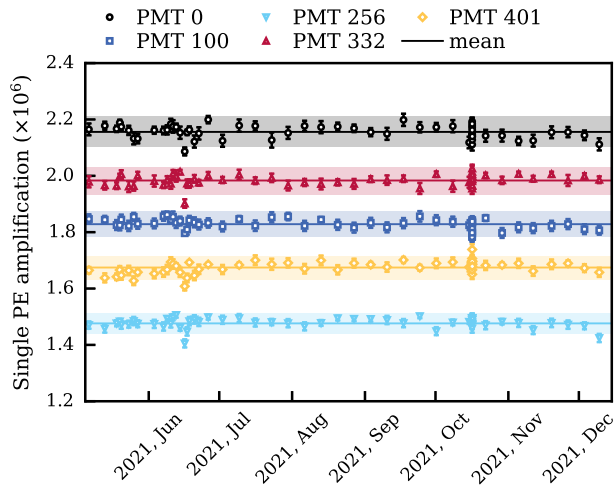


FIG. 2. Evolution of single-photoelectron amplification during SR0. The dense segment in June corresponds to radon calibration, involving multiple PMT calibration sessions. The high-density region around October corresponds to a dedicated calibration campaign focusing on evaluating the systematic uncertainty in gain computation. The displayed PMTs reflect the observed behavior in SR0, demonstrating, on average, stable gains with fluctuations confined to 2.5% highlighted by colored bands.

401), which are indicative of the behavior observed in the majority of PMTs within the XENONnT TPC. Modeling the gain evolution is based on a linear fit of successive subsets of adjacent gain calibration data points after smoothing the latter with a custom Savitzky-Golay filter [27]. The deviation between the measured and modeled gains consistently remained below  $\sim 2.5\%$  for approximately 93% of all sensors.

A total of 17 out of 494 PMTs were excluded from the SR0 analysis due to high electronic noise (1), unstable behavior (1), light emission (2), increasing afterpulse rate (11), and damage to the cable connection (2).

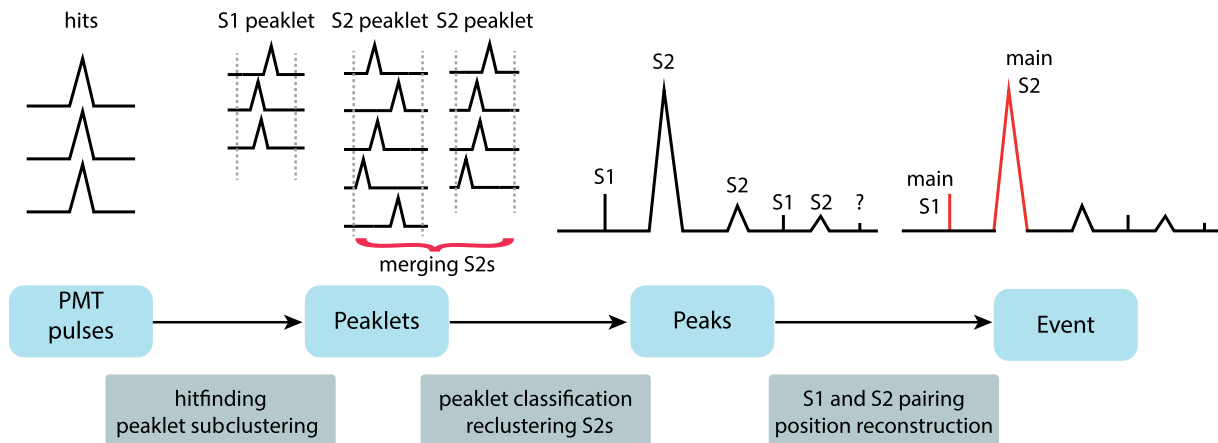


FIG. 3. The working principle applied in STRAXEN to build (S1, S2) events starting from PMT pulses and passing through intermediate objects (blue tiles). Reconstructed peaklets which do not satisfy either S1 signal classification or S2 signal classification are represented in the schema by the “?” label. The main processing steps are reported (gray tiles). Diagram adapted from [30] and from [31].

The stability of S1 and S2 signals over time is ensured by regularly monitoring the evolution of light and charge yields (LY and CY, respectively), discussed in Sec. VII, using data from monoenergetic sources spanning from 9.4 keV ( $^{83\text{m}}\text{Kr}$ ) to 5.6 MeV ( $\alpha$  from  $^{222}\text{Rn}$ ). Throughout blinded data acquisition, the LY and CY values demonstrated remarkable stability, with their deviations from the mean not exceeding 1% and 1.9%, respectively, as detailed in [28].

### III. SIGNAL RECONSTRUCTION AND SIMULATION

The scintillation light of the S1 and S2 signals liberates photoelectrons from the PMT photocathodes, which create a pulse that is digitized by the triggerless XENONnT data acquisition (DAQ) [29]. Each signal that passes a channel-dependent threshold is digitized at a sampling rate of 100 MHz, with the digitization period dynamically extended as long as the signal remains above the threshold, ensuring no data are lost. The entire stream of data from the PMTs is stored on disk long-term without further trigger, processing, or triage of the raw data. This enables us to reprocess the data with new algorithms or improved detector understanding at any given time. The reconstruction chain, shown in Fig. 3, aims to extract and match the S1 and S2 signals from the data stream.

#### A. Reconstruction chain

The reconstruction algorithms search for signals in the PMT waveforms. The time intervals of these signals are called “hits” and are defined as the time interval above threshold extended by a window of 30 ns on the left and 200 ns on the right. These per-PMT hits are sequentially grouped with neighboring hits in time (from any PMT) into clusters, where the time gap between consecutive hits

within a cluster is 700 ns or less. Isolated hits (“lone hits”), which have no neighboring hits in this time window, are primarily due to afterpulses or dark counts and are handled and stored separately. The clustered groups of hits are iteratively split into subclusters based on their timing information and the summed waveform of all hits in the cluster using a natural break algorithm [32]. This splitting is necessary to separate S1 signals from PMT afterpulses or nearby peaks. Subclusters exhibiting saturation are corrected based on the method developed in XENON1T [33] using a pulse model built from the nonsaturated channels.

These subclusters, called “peaklets,” are sequentially classified as S1 or S2 peaklets based on their waveform shapes along the classification boundaries shown in Fig. 4. These boundaries are encoded in the reconstruction software STRAXEN [34]. The boundaries and classification utilize several characteristics of the peaklets.

- (i) The *area* of the peaklet is the total charge (gain corrected, in PE) measured by all PMTs during the peaklet.
- (ii) The *rise time* is defined as the time between the 10% and the 50% area quantiles of the sum waveform. The 10% and 50% area quantiles are obtained from the time intervals commencing at the start of the first contributing hit, wherein 10% and 50% of the total charge of the peaklet is achieved, respectively.
- (iii) The *width* of the peaklet is the time range where the central 50% of the area of the peak resides.
- (iv) The *tight coincidence* (TC) is the number of different PMTs that have a hit within  $\pm 50$  ns around the time of the peaklet’s maximal amplitude.
- (v) The *area fraction top* (AFT) is the fraction of the total area seen in the top PMT array.

To be classified as S1, peaklets must lie below the two dashed lines shown in Fig. 4. There, the signals with fewer than 100 PE are displayed, while for larger signals, the rise time as a function of the area threshold increases to 200 ns. S2 signals originating from interactions at the bottom of the detector exhibit a larger temporal spread due to longitudinal diffusion during the electron cloud drift. Thus, S2 peaklets from a few electron signals may have been mistakenly split during the first stage of the peaklet building. Consequently, a merging step is applied to S2 peaklets using a gap-size clustering [34]. Adjacent S2 peaklets are merged until the combined duration exceeds 50  $\mu$ s or no further candidates are nearby. This cap prevents the inclusion of secondary delayed electrons and photoionization electrons, which are additional electrons freed via photoemission, into the main S2 peak. The allowable gap size for merging depends on the integrated peak area of the resulting S2. If any lone hits fall within the duration of the newly merged S2 peaklet, they are also included to avoid depth-dependent area bias for small S2 signals. Following this step, all merged S2 peaklets, along with unmerged peaklets such as S1’s or S2’s without a merging partner, are referred to as “peaks.”

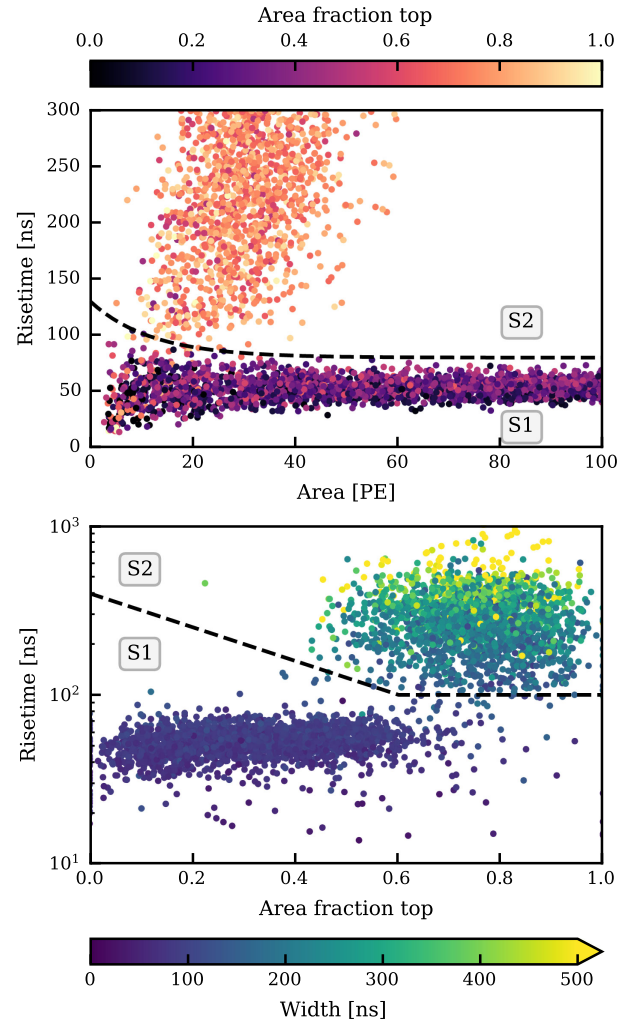


FIG. 4. Classification boundaries in STRAXEN [34] between S1 and S2 signals using the peaklets characteristics, showing the S1/S2 classification boundaries in area versus rise time (top) and area fraction top versus rise time (bottom): These are two-dimensional projections of a multidimensional parameter space. Only signals with less than 100 PE are shown. For values above this threshold, the rise time requirement as a function of area increases to 200 ns. The data shown are S1 peaks from a  $^{220}\text{Rn}$  calibration and isolated single electrons (the smallest S2 signals). S1 signals are typically much faster (i.e., have a shorter rise time) than secondary scintillation; this property is used in the top panel to discriminate between the two signals. S1 signals are expected to be measured predominantly by the bottom PMT array, while secondary scintillation light is produced in the xenon gas and, therefore, detected mostly by the top array. Furthermore, to minimize the number of fake S1 signals from accidental coincidences between PMT dark counts, a minimum of three PMTs must contribute to the tight coincidence window for the peaklet to be classified as S1 signal. Figure adapted from [35].

After defining S1 and S2 peaks from the PMT waveforms, the reconstruction algorithms build events from peaks. As there is no global trigger enforced at the DAQ [29], there is no predetermined event definition

(in contrast to XENON1T [36]). Events are built from the stream of peaks and are defined as the time region spanned around S2 signals with an area  $\geq 100$  PE, called the “triggering peak.” Additionally, the triggering peak must have fewer than eight other neighboring peaks in a window of  $\pm 10$  ms that have  $> 50\%$  of the area of the triggering peak (called the “n\_competing” requirement). This requirement ensures that only the largest S2 signals act as triggering peaks and that, e.g., continued photoionization tails and delayed electrons after large S2 signals do not lead to a high number of triggering peaks. Events are defined as the time window encompassing 2.45 ms prior to and 0.25 ms after the triggering peak. If multiple event windows overlap, they are merged. The primary S1 is identified by the largest S1 peak within the event window, whereas the main S2 peak is determined by the largest S2 signal detected after the main S1. The second largest S1 (S2) peak within an event are designated as “alternative” S1 (S2). Similarly, the alternative S2 must be recorded following the main S1. Identifying these alternative peaks is crucial for recognizing multiscatter events.

The n\_competing requirement leads to an energy-dependent event-building efficiency. Considering the *high* single-electron rate, it is likely that a signal’s S2 occurs near many single electrons and cannot trigger the event consequently. This efficiency is computed as a function of the S2 signal using the simulation framework. For the S2-area threshold of 500 PE used for the ER search [9], the event-building efficiency is 99.3%. For the WIMP search [5], the threshold is 200 PE, corresponding to an efficiency of 97.2%. These efficiencies are accounted for in the inference [8].

## B. Signal simulation

Monte Carlo (MC) simulations of the detector response to S1 and S2 signals are performed to understand potential biases and inefficiencies. The simulation work flow, starting from the photon and electron yields up to DAQ simulation, is managed using the waveform simulator (WFSim) package [37].

The simulation work flow can integrate with the XENONnT simulation package [38] based on the Geant4 toolkit [39,40] to generate the necessary energy depositions. The modeling of liquid xenon response to the deposited energy is the first step of the simulation pipeline. The EPIX (electrons and photons instructions for XENON) package [41] processes energy depositions to evaluate primary scintillation photons and electrons yield per interaction, using models from the Noble Element Simulation Technique (NEST) software [42].

The light quanta derived from EPIX are used to generate detected photon arrival times per PMT necessary to simulate S1 signals. The photon scintillation delay times are generated using NEST. The per-PMT hit distribution as well as the time delay from optical propagation are then

produced based on a precomputed probability map obtained from optical simulation. These optical simulations are performed with Geant4 using a TPC model whose optical properties are derived by matching the MC simulation to  $^{83\text{m}}\text{Kr}$  calibration data, as detailed in [30].

To simulate S2 signals, the first step consists of modeling the electron drift using a precomputed electric field map [14]. The processes of electron diffusion and losses to electronegative impurities are also accounted for when evaluating the number, time, and position of electrons reaching the gate electrode. The probability of an electron being extracted from liquid xenon to the gas amplification phase is derived from a data-driven map. For each electron extracted in the gas phase, we estimate the number of photons detected, depending on its position, arrival time in the gas, and the measured secondary gain (PE measured per electron drifting in the gas phase). As for S1 simulations, the detected photon arrival times per PMT are obtained from optical simulations. The final photon hit times are generated by summing the initial electron arrival time with a sampled atomic excitation time, scintillation delay, and optical propagation delay.

For each of the generated PMT hits, the PMT and DAQ readout responses are applied, accounting for pulse shape and amplification with data-driven templates, digitizer threshold value, sampling rate, and electronic noise from prerecorded samples. This results in simulated pseudodata in the same format as provided by our real detector so that the same data processing work flow can be used for its analysis. More details about this waveform emulating framework can be found in [43]. This full-chain simulation work flow is used to evaluate reconstruction efficiency and its bias, to complement the information extracted from calibration data.

## C. Reconstruction efficiency

The reconstruction efficiency is the probability that a given peak is reconstructed with the proper classification. The main mechanism of S1 reconstruction efficiency loss arises from the S1 classification (Fig. 4). For the first XENONnT analysis in SR0, as stated in Sec. III A, hits in at least three distinct PMTs within the TC window of the peak are required. This criterion is particularly effective at low energies, where it significantly reduces accidental coincidence events caused by dark counts or electronic noise misidentified as S1 signal and paired with a lone S2 signal. The second constraint impacting the accurate classification of S1 signals involves the rise time and AFT boundaries, designed to distinguish between S1 signals and single electrons (SE), as shown in Fig. 4. Since S1 photons often undergo total reflection at the liquid-gas interface, S1 signals originating from the upper part of the LXe volume exhibit a broader time profile due to an increased number of reflections and scattering inside the TPC. To quantify the detection efficiency, S1

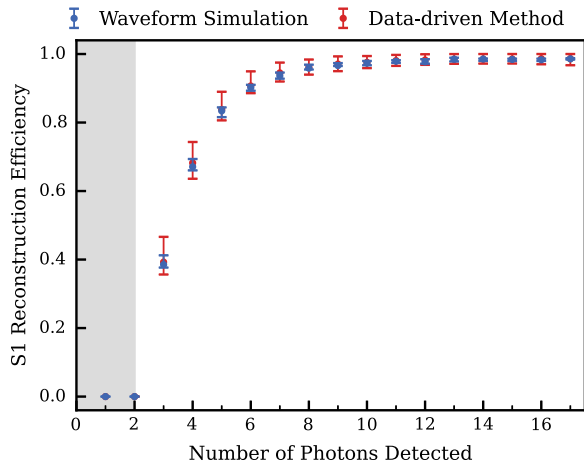


FIG. 5. S1 reconstruction efficiency as a function of number of detected photons. The red and blue markers show the median detection efficiency for both data-driven and simulation methods. The gray band below three photons detected marks the undefined region for S1 when requiring a tight coincidence of at least three PMTs. The uncertainty for the data-driven method is mainly a combination of data-selection bias, energy, and position dependence of S1 pulse shape together with statistical uncertainty. The uncertainty for the waveform simulation method is dominated by position dependence in the S1 pulse shape. The final results are based on waveform simulation, while the data-driven method serves as a cross-check.

signals are simulated using `WFSim`. While incorporating a  $Z$ -dependent S1 detection efficiency into the detector response model could accurately reflect this aspect, such an approach is computationally intensive. Therefore, the  $z$  dependence is alternatively represented as a systematic uncertainty ( $< 5\%$ ) on the efficiency.

The S1 detection efficiency is shown in Fig. 5. The simulation-driven method discussed above was cross-validated using a data-driven method, also shown in Fig. 5. In the data-driven method, a subset of photon hit waveforms from larger parent S1 peaks in data are sampled to form smaller S1 signals. These are then processed by the reconstruction software to find S1 peaks. The parent S1 pool is a mixture of S1 peaks from  $^{37}\text{Ar}$  and  $^{83\text{m}}\text{Kr}$  calibration data. The uncertainty band for the data-driven method originates from a combination of data-selection bias, energy and position dependence of the S1 pulse shape, and statistical uncertainty. The uncertainty band for the simulation method is dominated by position dependence in the S1 pulse shape.

The S2 efficiency is determined based on a similar simulation-driven procedure. Above 200 PE, the lowest S2 threshold used, the S2 efficiency is  $> 99\%$ .

#### D. Peak reconstruction bias

The area ( $A$ ) of a peak is the sum of the gain-corrected measured charge in the PMTs, quantified in number of PEs. The reconstruction error  $\phi$  is expressed as the discrepancy

between the input area ( $A_{\text{sim}}$ ) and the output reconstructed area ( $A_{\text{rec}}$ ):

$$\phi = \frac{A_{\text{rec}} - A_{\text{sim}}}{A_{\text{sim}}}, \quad (1)$$

where  $A_{\text{rec}}$  corresponds to the simulated peak area after processing it with the signal reconstruction framework STRAXEN. Several effects contribute to a nonzero value of  $\phi$  for a S1 or S2 peak.

- (i) The PMT response to single photon-electron signal can be underamplified, yielding a negative error in the reconstructed area.
- (ii) The per-PMT DAQ digitization threshold prevents very small signals, which might be noise or irrelevant, from being registered. In STRAXEN, the hit finder threshold works similarly and can result in a negative error.
- (iii) Electronic noise can distort a signal, which can result in a positive or negative error.
- (iv) PMT afterpulses and photoionization, when merged with their progenitor peaks, will yield a positive error.
- (v) The reconstruction software may reconstruct signals too small or too large, for example, if a portion of the signal is wrongfully not considered part of the peak.

The reconstruction bias is expressed as the median of the  $\phi$  distribution. The bias is estimated by simulating S1 and S2 peaks that are spatially uniformly distributed. The results, showing the median and its  $1\sigma$  quantiles, are presented in Fig. 6. At low energies, S1 signals exhibit a bias of  $-2\%$  due to the digitization threshold and PE underamplification. This bias exhibits a large spread, as indicated by the  $1\sigma$  ranges, which stems from electronic noise and limited statistics. Conversely, at higher energies, an increasing trend in S1 bias is noted, primarily due to the inclusion of afterpulses. Similarly, for S2 signals, the inclusion of afterpulses results in a positive bias at higher energies. At lower energies ( $A_{\text{sim}} < 10^4$  PE), S2 signals show a negative bias, again influenced by the digitization threshold. The bias trends for S2 are otherwise similar to those observed for S1. This peak reconstruction bias study is discussed in more detail in [35].

These biases in S1 and S2 signal reconstruction, alongside the S1 reconstruction efficiency, are input parameters for the signal and background response models [8] and for the energy reconstruction methodology outlined in Sec. VII.

## IV. POSITION RECONSTRUCTION

An accurate position reconstruction is crucial for background model building [8] and proper signal corrections. The self-shielding effect of LXe keeps radiogenic backgrounds mainly near the edge of the detector, which can be rejected by selecting a restrictive fiducial volume (see

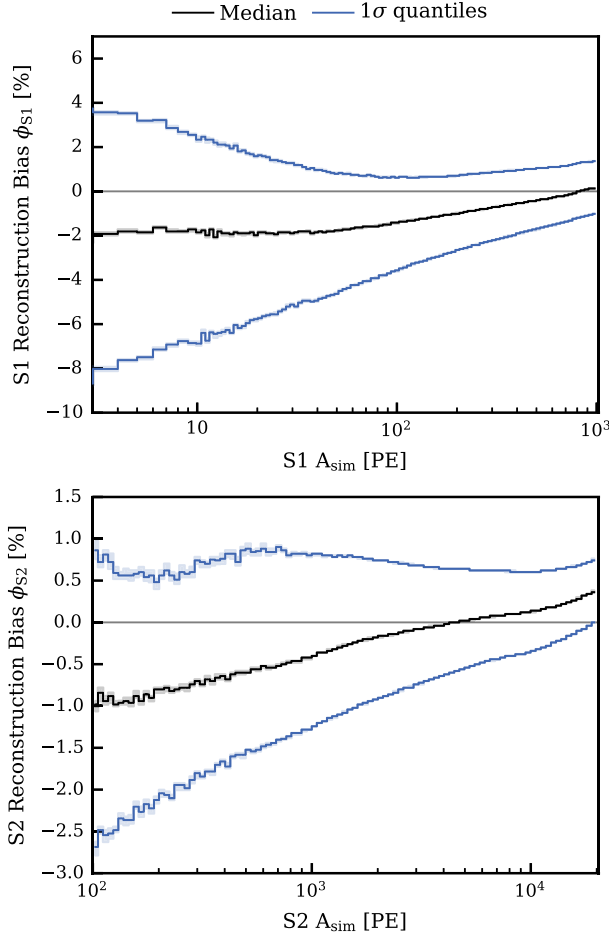


FIG. 6. Reconstruction bias for S1 (top) and S2 (bottom) signals, calculated according to Eq. (1), plotted against the simulated signal area  $A_{\text{sim}}$  with a threefold tight coincidence requirement. The reconstruction bias corresponding to the median error is shown by the black line, with the  $1\sigma$  variation depicted by the blue lines. The shaded bands represent the uncertainties of the quantiles from bootstrapping.

Sec. VII). Accurate energy reconstructions require position-dependent S1 and S2 corrections (see Sec. V).

### A. 3D position reconstruction

The vertical position of an event ( $Z_{\text{obs}}$ ) is obtained by the time difference between its corresponding S1 and S2, namely, drift time ( $\Delta t_{\text{drift}}$ ), multiplied by the expected electron drift velocity, measured *in situ* to be  $(0.675 \pm 0.006)$  mm/ $\mu$ s at 23 V/cm. The reference depth zero point ( $Z = 0$  cm) is set at the bottom of the gate electrode, and the maximum drifting distance is set to be  $Z = -148.65$  cm, corresponding to the top of the cathode electrode.

The horizontal position ( $X_{\text{obs}}, Y_{\text{obs}}$ ) is obtained from the S2 signal's hit pattern on top PMT array by machine-learning-based models trained on simulated events. Three independent algorithms were developed using

TensorFlow [44]: one based on a multilayer perceptron (MLP), one on a convolutional neural network (CNN), and a third on a graph-constrained network (GCN) [45]. All three algorithms were trained on hit patterns from a full-chain simulation with realistic detector conditions, such as real-time PMT gain values and exclusion of problematic PMTs, as described in Sec. II B. The top light pattern normalized by the maximal PMT signal, which was found to give the best reconstruction performance, is then fed into the models to calculate the horizontal position of an event.

The three algorithms reconstructed most events at the same locations, with differences smaller than a few millimeters. This difference between reconstructed positions is used as an event quality criterion (see Sec. VI C). Unless stated otherwise, MLP-based results were used as the default event positions for corrections and analyses since these provided the best resolution.

### B. Position resolution

The position resolution primarily depends on the size of S2 signals or, more specifically, the size of the top PMT's responses to S2 signals, called  $S2_{\text{top}}$ . Regions around turned-off PMTs and near the edge of the TPC show worse resolution due to reduced sensors proximity and photon reflections on the PTFE wall.

With the full chain simulation described in Sec. II B, the position resolution was calculated by comparing the true positions of simulated data and reconstructed positions. This is expressed by the standard deviation  $\sigma_R$  of the differences, shown in Fig. 7 as a function of  $S2_{\text{top}}$ . Within a radius of 60 cm, for the lowest-energy S2's around 100 PE, the resolution was estimated to be around 1.5 cm for GCN and MLP and 1.9 cm for CNN. In contrast, for large S2 signals ( $\geq 10^4$  PE), the resolution improves to less than 0.25 cm for all three position reconstruction algorithms.

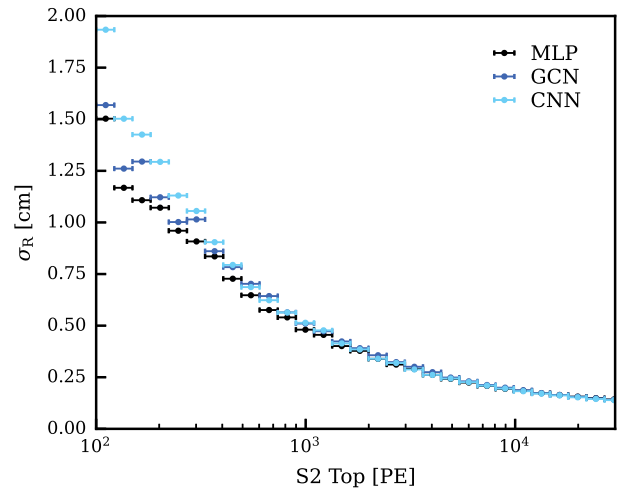


FIG. 7. Simulation-driven estimate of the radial resolution in the inner part of the TPC for the three position reconstruction algorithms used in this work within a radius of 60 cm.

At the edge of the sensitive volume, due to reflections on PTFE adding uncertainties in S2 hit patterns, the event resolution is approximately 1.5 times worse for small S2 signals and 2 times worse for large S2 signals compared to events occurring near the center.

### C. Field distortion correction

Because of the low field, the discreteness of field-shaping rings, and negative charge buildup on PTFE walls, the drift field was deformed, resulting in a depth-dependent inward bias of the reconstructed S2 position [14]. As shown in the left canvas in Fig. 8, while  $^{83\text{m}}\text{Kr}$  events should be evenly distributed inside the TPC, events from the bottom were observed more concentrated toward the center as electrons follow the distorted drift field lines. The two distinctive linear features in the  $(X_{\text{obs}}, Y_{\text{obs}})$  distribution of  $^{83\text{m}}\text{Kr}$  events, shown in Fig. 8, were caused by the electric-field-channeling effect from additional transverse wires on the gate and anode grids. Moreover, the transversal stride pattern is likely due to the partial shadowing of the top PMT array by anode wires.

The utilization of wired electrodes added complexities in electric field simulation, making the development of a simulation-driven correction challenging near the transversal

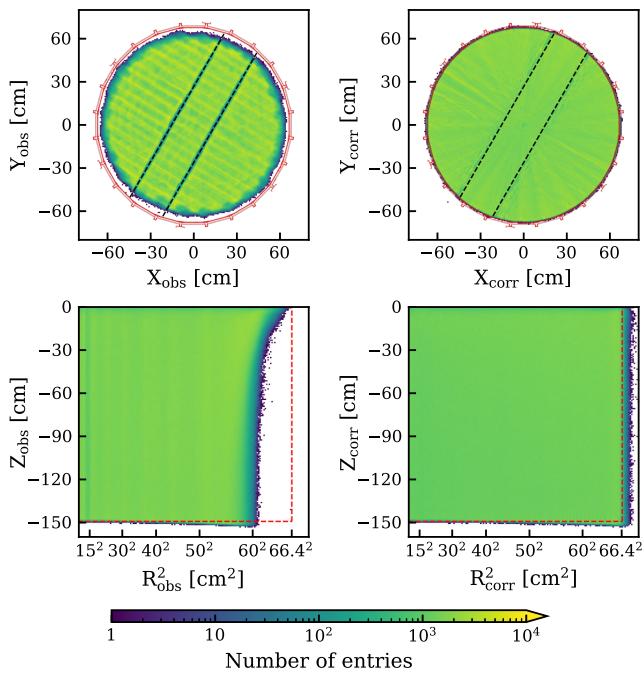


FIG. 8. Reconstructed spatial distributions—from MLP algorithms—of  $^{83\text{m}}\text{Kr}$  events in the  $(X, Y)$  space (top) and  $(R^2, Z)$  space (bottom) and pre- (left) and post-field-distortion correction (right). In the  $(X, Y)$  space, the positions of PTFE panels and pillars are illustrated in red, while the black dashed lines indicate the transverse wires installed on the gate electrode. The  $(R^2, Z)$  space includes the cathode position and the PTFE walls in red dashed lines as constraints on the sensitive volume of the TPC.

wires. To address this, a purely statistical approach, similar to the one used in XENON1T [26], was adopted. This method relies on the fact that  $^{83\text{m}}\text{Kr}$  events are uniformly distributed across the radial position within the TPC. Because electric field lines do not cross, to correct for distortions, each observed radius ( $R_{\text{obs}}$ ) and its corresponding percentile in the whole population along the radial line can be mapped to an evenly distributed scale from the origin to the TPC's inner wall radius ( $R_{\text{wall}} = 66.4$  cm). The detector was segmented into pie slices based on drift time ( $\Delta t_{\text{drift}}$ ) and observed azimuthal angle ( $\varphi_{\text{obs}}$ ). Given that the electric field at the top of the TPC is more disturbed due to its proximity to the electrodes, whereas the field at the bottom is more homogeneous, finer  $\Delta t_{\text{drift}}$  binning was taken at the top. Within each  $\Delta t_{\text{drift}}$  slice, the detector was further divided into sections based on  $\varphi_{\text{obs}}$ . The field distortion correction was further validated by analyzing the reconstructed position distributions from external calibration sources, which do not rely on the assumption of uniformity.

In XENON1T, the  $Z_{\text{obs}}$  position was corrected using a geometric relation that assumes the electron cloud trajectory is a straight line from the interaction vertex to the extraction point [26]. However, in the case of XENONnT, this assumption does not hold, especially near the very top edge of the TPC where the field is nonuniform due to the configuration of the field-shaping rings, and the perpendicular wires cause deviations in the electron path on the order of a few centimeters [14]. No correction is applied here to the  $Z_{\text{obs}}$ , with the uncorrected bias less than 1 cm at the bottom and near the edge of the detector.

## V. SIGNAL CORRECTIONS

The reconstructed S1 and S2 signals have spatial and temporal dependences influenced by detector effects such as electric field inhomogeneities, light absorption, and xenon purity. The detector conditions and signal responses were studied, aiming to understand them and develop corrections to ensure a homogeneous response.

The final impact of the XENONnT SR0 analysis corrections is illustrated using  $^{83\text{m}}\text{Kr}$  calibration data in Fig. 9: An average improvement of  $\sim 20\%$  in signal resolution has been estimated using S1 and S2 signals from the krypton calibration data. In the rest of this section, we will introduce the relevant corrections in detail.

### A. S1 signal correction

At a given location within the detector in cylindrical coordinates  $(R, \varphi, Z)$ , the observable photon count is contingent upon several efficiencies: The photon yield (PY) represents the number of photons produced per unit of energy  $\varepsilon$  under a specific drift field  $E_{\text{drift}}$ ; the light collection efficiency  $\epsilon_L$  indicates the proportion of emitted photons that arrive at a PMT photocathode; the quantum efficiency  $\epsilon_{\text{QE}}$  of the PMT is the probability for the incident

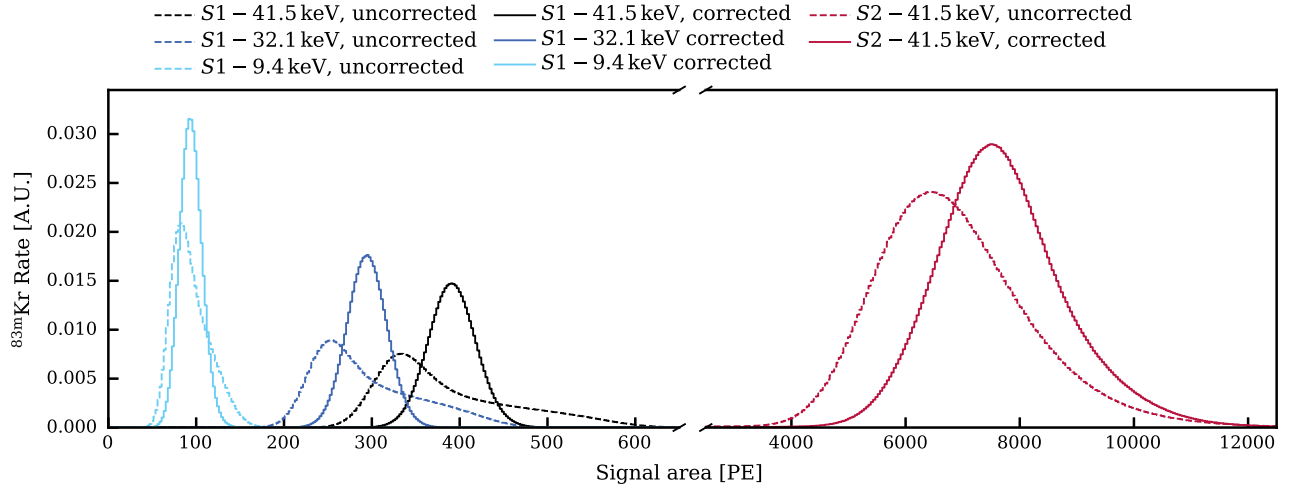


FIG. 9. Comparative display of the  $^{83\text{m}}\text{Kr}$  S1 and S2 signals pre- and postcorrection in dashed and solid lines, respectively.

photon to be converted to a photoelectron by the photocathode; and the PMT collection efficiency  $\epsilon_{\text{CE}}$  reflects the efficiency with which PEs are gathered within the PMT itself. These factors collectively determine the LY, i.e.,  $\langle \text{S1} \rangle$ , denoting the number of detected PE per unit of deposited energy in the detection medium:

$$\begin{aligned} \text{LY}(\mathbf{R}, \varphi, Z, \epsilon) &= \frac{\langle \text{S1} \rangle(\mathbf{R}, \varphi, Z, \epsilon)}{\epsilon} \\ &= \epsilon_L(\mathbf{R}, \varphi, Z) \cdot \text{PY}(\epsilon, E_{\text{drift}}(\mathbf{R}, \varphi, Z)) \cdot \epsilon_{\text{QE}} \cdot \epsilon_{\text{CE}}. \end{aligned} \quad (2)$$

It should be noted that  $\epsilon_{\text{QE}}$  and  $\epsilon_{\text{CE}}$  vary by PMTs and, thus, have spatial dependence. Besides, these factors depend on the physical position where the energy deposition happens. Therefore, the coordinates used in Eq. (2) are the field-distortion-corrected positions as discussed in Sec. IV C. To enhance readability, we will omit *corr* in the subscript for the remainder of this section. The light collection efficiency and field inhomogeneities induce a spatial dependence of the amount of photons collected from the S1 signals. A three-dimensional correction map is derived from the 41.5 keV signals in  $^{83\text{m}}\text{Kr}$  calibration data to correct for these spatial dependencies. This process necessitates an initial decoupling of effects due to drift field inhomogeneities, which are energy dependent, from those stemming from the geometric efficiency of light collection, which are not.

As a preliminary step, the  $\text{S1}_{\text{fec}}$ , representing the field-effect-corrected S1 signals, is calculated. This correction, formulated in Eq. (3), involves normalizing the S1 signals by the relative PY derived from the XENONnT electric field [14] and the PY field-dependent model measured in Ref. [46]. The PY at any given position is adjusted relative to the PY corresponding to the average drift field in the TPC, set at  $\langle E_{\text{drift}} \rangle = 22.9$  V/cm:

$$\text{S1}_{\text{fec}}(\mathbf{R}, \varphi, Z) = \text{S1}(\mathbf{R}, \varphi, Z) \cdot \frac{\text{PY}(\epsilon, \langle E_{\text{drift}} \rangle)}{\text{PY}(\epsilon, E_{\text{drift}}(\mathbf{R}, \varphi, Z))}. \quad (3)$$

To construct the S1 correction map  $L_c(\mathbf{R}, \varphi, Z)$  as defined in Eq. (4), the TPC is segmented into bins with equal volumes:

$$L_c(\mathbf{R}, \varphi, Z) = \frac{\text{LY}(\mathbf{R}, \varphi, Z, \epsilon, E_{\text{drift}})}{\langle \text{LY}(\epsilon, E_{\text{drift}}) \rangle} = \frac{\text{S1}_{\text{fec}}(\mathbf{R}, \varphi, Z)}{\langle \text{S1}_{\text{fec}} \rangle}. \quad (4)$$

The number of bins of the correction map is optimized in each dimension to limit the maximum statistical uncertainty to 2%. For each bin, the average  $\text{S1}_{\text{fec}}$  is normalized against the mean  $\text{S1}_{\text{fec}}$  observed in the central region of the TPC, defined by the boundaries  $-130$  cm  $< Z \leq 20$  cm and  $R < 50$  cm. The resultant map, depicting the relative LY in the detector, is illustrated in Fig. 10.

In addition to spatial dependencies, temporal variations in PMT performance influenced the measurements of both S1 and S2 signals. A notable fluctuation in the area of lone-hit signals, depicted in the first panel in Fig. 11, was observed during the initial calibration phase of SR0. This variation stabilized in the subsequent blinded data-taking period. The evolution of the median lone-hit area during the calibration period exhibits two distinct trends. First, a long-term decreasing trend was noted, the exact cause of which remains elusive. However, it is likely attributable to variations in detector conditions, such as temperature and pressure, observed during the same calibration period, which could impact the PMT response. Second, short-term fluctuations were detected during calibration periods, coinciding with the PMTs being periodically turned off and on for the injection of  $^{220}\text{Rn}$  sources.<sup>2</sup> A relative

<sup>2</sup>To protect PMTs from the initial high burst of alpha particles in the gas phase after each  $^{220}\text{Rn}$  source injection.

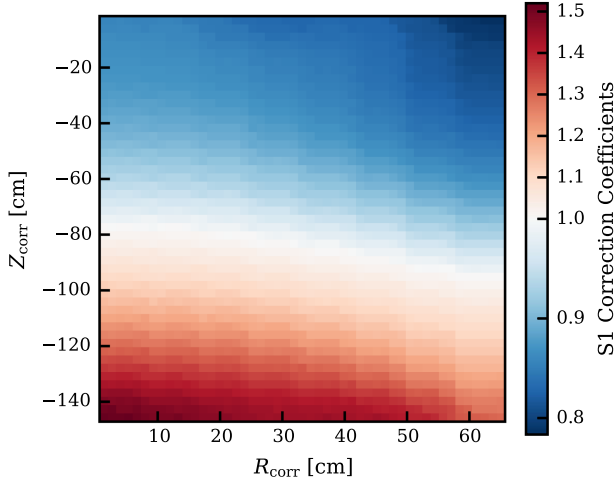


FIG. 10. Map of relative light yield extracted from  $^{83\text{m}}\text{Kr}$  calibration data, employed for the S1 correction in SR0. The white region indicates the reference location where the correction factor is 1. The color scale is linear, with different slopes above and below 1.0 to accommodate the asymmetry in the relative light yield distribution.

empirical correction is defined based on the temporal evolution of the median lone-hit area for SR0 PMTs, noted  $LH_c(t)$ , normalized against the stable median area observed during the blinded data-taking phase at  $LH_0 = 1.07$  PE. The corrected S1 signal, cS1, after spatial and time-dependent corrections are applied, is computed following Eq. (5):

$$\text{cS1} = \frac{\text{S1}(\mathbf{R}, \varphi, Z, t) \cdot LH_0}{L_c(\mathbf{R}, \varphi, Z) \cdot LH_c(t)}. \quad (5)$$

### B. S2 signal correction

To ensure accurate and unbiased energy reconstruction, a given energy deposition should always result in the same S2 area, up to some statistical fluctuations. However, due to detector geometry, PMT responses, imperfect electric fields, etc., the areas of S2 signals show a strong spatial dependence. To remove these detector effects, S2 signals from a monoenergetic  $^{83\text{m}}\text{Kr}$  source were used to generate a correction map to be applied to all observed events and mitigate such instrumental spatial dependence. This correction is referred to as the S2 position-dependent correction.

To protect the PMT arrays from potential damage caused by high-intensity single-electron burst events, the gate and anode electrodes were occasionally ramped down when such events occurred during data taking. In close correlation to these ramping-down activities, we observed variations in the S2 yield per electron, called single-electron gain (SEG), and a reduction in the fraction of electrons extracted from the liquid to the gas phase, called extraction efficiency (EE), which could be related to the disturbance of the

electric field resulting from a relaxation of electrostatic forces. Such a dynamic response of the detector is visible up to three days after each ramp-up. Since only relative changes affect the cS2 values, SEG and EE were normalized and implemented as corrections, which we call the S2 time-dependent corrections.

#### 1. S2 position-dependent correction

There are two major components for S2 position-dependent corrections: the electron lifetime (EL) correction, which handles the attenuation when electron clouds drift up in the detector, and the S2(X, Y) correction, which eliminates effects from nonuniform extraction fields due to electrodes sagging or detector tilting and nonuniform light collection. Since the phenomena corrected by S2(X, Y) all relate to the location of the electron extraction site, the correction depends on the observed location of events, labeled  $(X_{\text{obs}}, Y_{\text{obs}})$ , rather than the inferred  $(X_{\text{corr}}, Y_{\text{corr}})$  of the initial energy deposition. To enhance readability, we will omit obs in the subscript for the remainder of this section.

The electrons inside the drifting cloud can attach to electronegative impurity sites. The resulting S2 attenuation is described by

$$\text{S2} = \text{S2}_0 \cdot \exp\left(\frac{-\Delta t_{\text{drift}}}{\tau_{\text{EL}}}\right). \quad (6)$$

In this equation,  $\tau_{\text{EL}}$  is the EL, while  $\text{S2}_0$  corresponds to the unattenuated S2 area at the interaction vertex depth ( $\Delta t_{\text{drift}} = 0$ ) before any signal attenuation. The EL is a measure of xenon purity and can be derived from the depth-dependent attenuation of the S2 signal in monoenergetic calibration sources. During SR0, the EL was monitored using  $^{83\text{m}}\text{Kr}$  and  $^{37}\text{Ar}$  calibration data and 5.6 MeV  $\alpha$  decays from emanated  $^{222}\text{Rn}$  present in the xenon target. The purity of the xenon target was further evaluated via a purity monitor: a 20-cm-long electron drift chamber in the purification system [13]. As for S1 signals, before conducting EL measurements, it is necessary to correct for the drift field's nonuniformity in the TPC. The EL evolution is depicted in the second panel in Fig. 11, with the agreement among the three internal sources and the purity monitor. The EL trends during SR0 display multiple sharp declines aligning with the release of impurities during operations on the xenon cryogenics and purification systems.<sup>3</sup> Furthermore, continuous outgassing of the materials and restricted xenon circulation flow in the purification systems led to a plateau in the EL after a certain period. The EL measurements in the TPC from  $^{83\text{m}}\text{Kr}$  and  $^{222}\text{Rn}$  data

<sup>3</sup>Such operations include the start of the Rn distillation column, or changes in the xenon purification circuit, which were necessary for the getter bypass mode at the end of SR0.

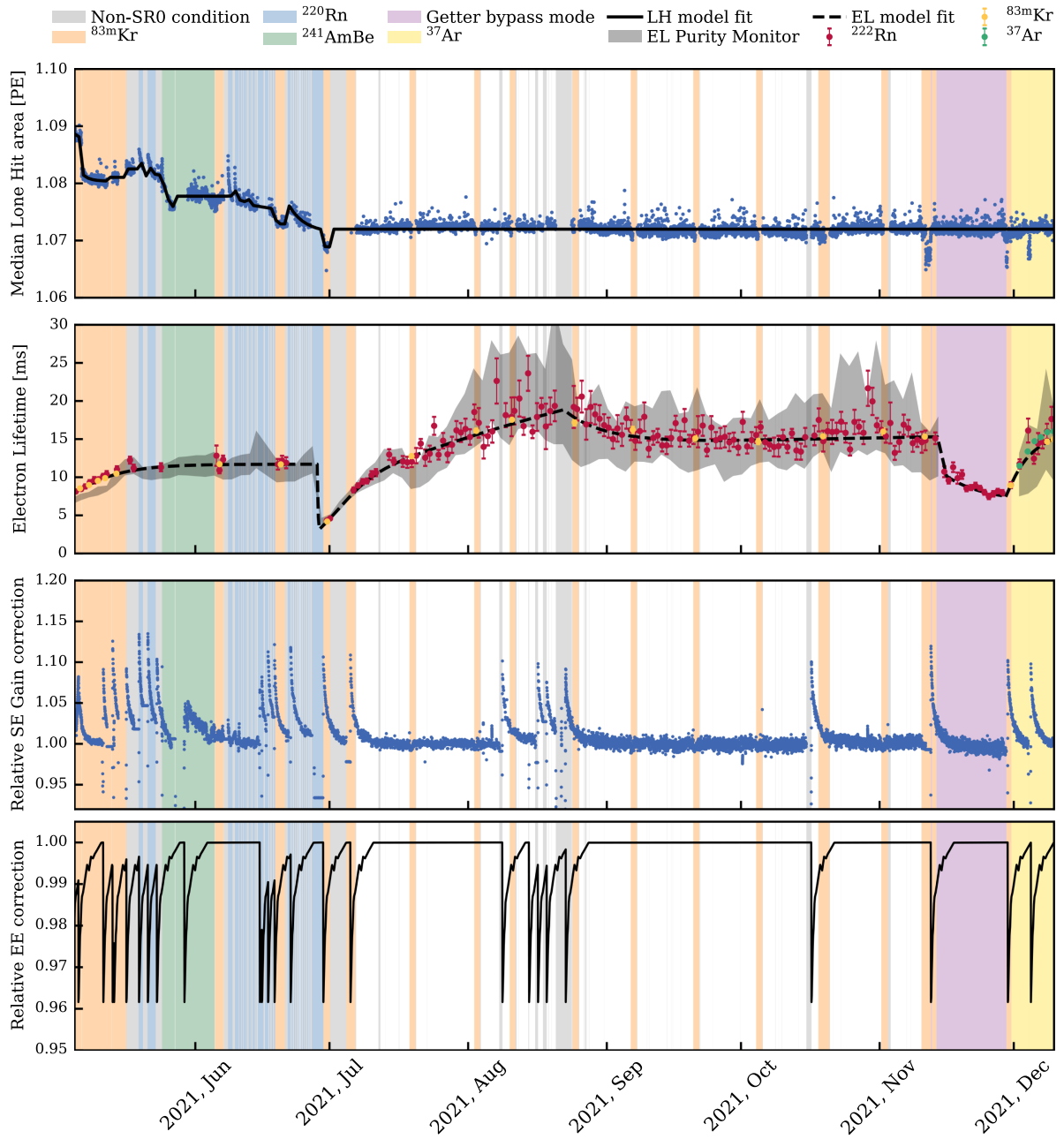


FIG. 11. SR0 timeline displaying (panel 1) evolution of median lone-hit area (see Sec. III A) in top and bottom PMTs, with the time-dependent empirical model used for lone-hit correction. (Panel 2) Electron lifetime model derived via  $^{222}\text{Rn}$  (red),  $^{83\text{m}}\text{Kr}$  (yellow), and  $^{37}\text{Ar}$  (green). The gray band is the measurement by the purity monitor with its systematic uncertainty. (Panels 3 and 4) Normalized single-electron gain (top) and relative extraction efficiency (bottom) variations, revealing peak structures attributed to the ramping down and up of the anode, induced by occurrences of electron bursts.

were collectively utilized to model the observed trends, represented by the black dashed line.

To make the S2 signals homogeneous in the XY plane, the  $^{83\text{m}}\text{Kr}$  calibration data with a total duration of half a month at the beginning of May 2021 were used. These data were divided into runs of 30 min. Within each run, the S2's from  $^{83\text{m}}\text{Kr}$  events were normalized to the mean value of the whole population to represent the relative S2 area as a

function of the xy position. Then, the whole (X, Y) plane ranging from  $-70$  to  $70$  cm in both directions were divided into  $100 \times 100$  bins, within each of which the S2 areas were averaged. This resulted in the expected relative S2 area associated with the (X) location at the center of the bin. The final S2(X, Y) correction map  $c(X, Y)$  was then obtained by averaging all the maps with weighted mean, with the number of events from each 30-min run. This method

avoids effects from the time evolution of S2 signals due to the electrode operations discussed in Sec. V B 2, and, thus, the map generated is decoupled from the time evolution corrections. The resulting S2 correction maps to  $S2_{\text{top}}$  and  $S2_{\text{bottom}}$  are shown in Fig. 12. A larger correction is

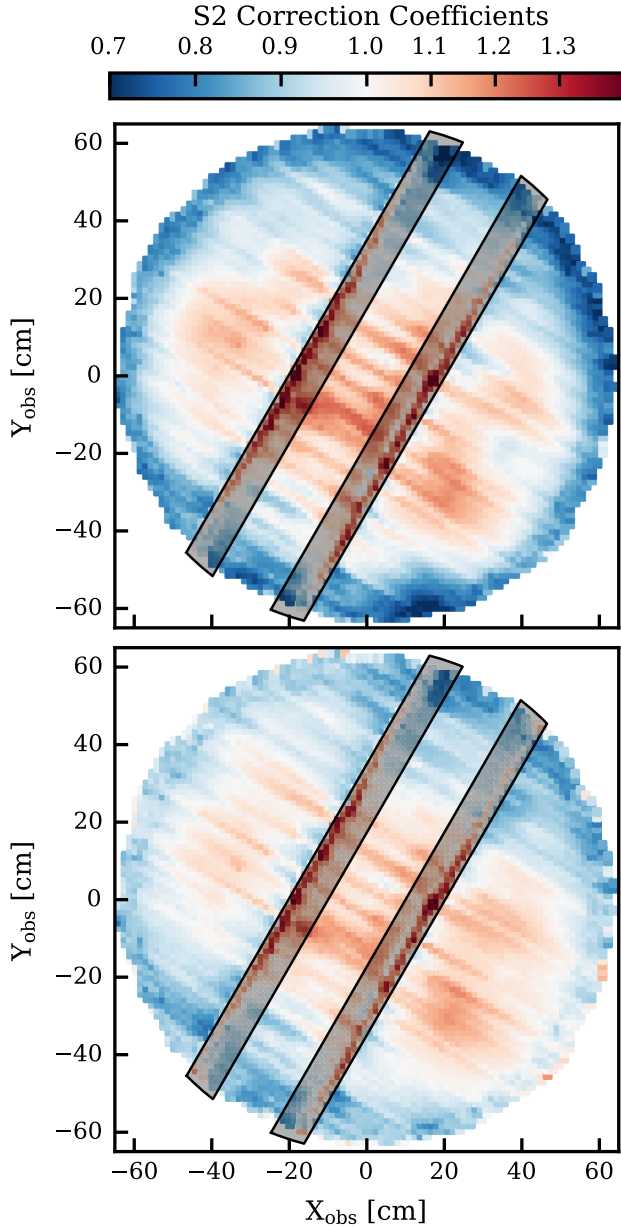


FIG. 12. Relative S2 correction maps extracted from  $^{83\text{m}}\text{Kr}$  events, used for S2 correction in XENONnT based on the observed position. The map shown in the top panel has been used to correct the S2 part collected by the top PMT array, whereas the bottom map for the S2 portion was recorded by the bottom PMT array. The white region indicates the reference location where the correction factor is 1. The color scale is linear, with different slopes above and below 1.0 to accommodate the asymmetry in the S2 correction coefficients. The near-wire region is shaded out.

required in the center of the TPC, owing to a localized extraction efficiency increase caused by the reduced distance between the electrodes as a result of the sagging of the electrodes. The transversal wires strengthen the extraction field around their locations in the gas gap between the anode and the gate, affecting the electron extraction efficiency and proportional scintillation, as discussed in [47]. This results in the requirement of exceptionally large ( $\sim 50\%$ ) corrections around the wire regions. Although the PMT responses for S2 signals at the bottom array are more nonlocalized compared to those at the top array due to the distance to the gas gap, such nonlocality smears away only PMT-dependent fluctuations, whereas the absolute S2 yield difference, especially the boost near the transversal wires, is originated from the difference in the number of photons generated by the electrons in the gas gap and should be observable from the responses of the bottom PMT array.

While physically decoupled, the developments of  $S2(X, Y)$  and EL corrections are correlated and dependent on each other. The method of decoupling the two was to find asymptotic behavior through iteration. Initially, the EL was calculated using uncorrected S2 signals. Following this, a preliminary  $S2()$  map was constructed. This map was then used to update the EL calculation. This process was iteratively repeated to refine both the map and the EL estimates. Both corrections reach stability after about eight iterations.

## 2. S2 time-dependent correction

The S2 time-dependent corrections have two components: the evolutions of SEG and EE. SEG can be obtained by tracking the S2's of the single-electron population. Two distinctive behaviors of SEG were observed inside the TPC: Between the gate transverse wires, there was a strong change in SEG after ramp-up, while outside it was stable. Such a behavior difference led to a partitioning inside the TPC as shown in Fig. 13. To normalize the SEG values to correction factors, SEG values between 2021-07-05 and 2021-08-08 were used, and two SEG values, respectively, in the two partitions, were set to be the reference SEG for SR0. The normalized SEG evolution for partition I (P-I) is shown in Fig. 11. No time variation was observed in partition II (P-II), so the correction factors were set to one (no correction), and, therefore, it is not displayed.

A relative extraction efficiency (REE) was calculated based on position-dependence-corrected [both  $S2(X, Y)$  and EL] S2 signals of  $^{83\text{m}}\text{Kr}$  events and the SEG for each run. By dividing SEG from position-dependence-corrected S2 signals of  $^{83\text{m}}\text{Kr}$  events, the expected number of electrons can be obtained from this monoenergetic source. The mean value of the expected number of electrons between 2021-07-05 and 2021-08-08 was used as a reference, and all other values were normalized to obtain REE. These were used to construct a model, as shown in the

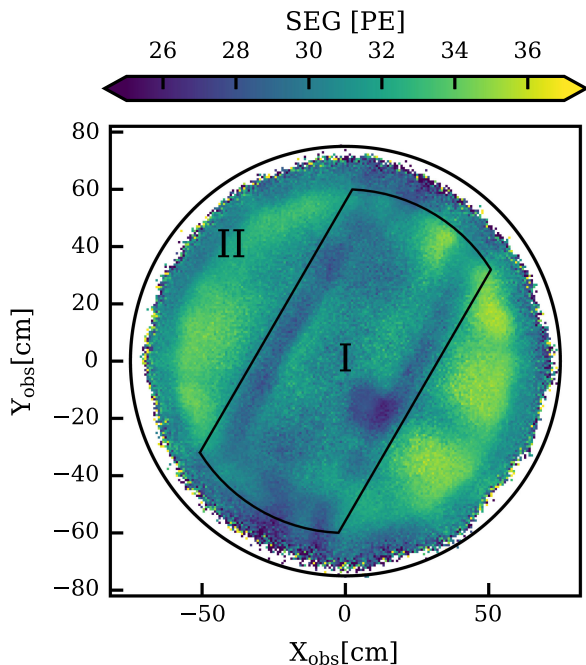


FIG. 13. Partitions of the TPC plane due to different single-electron gain and relative extraction efficiency responses after each ramp-up of electrodes, overlaid with the SEG X-Y distribution. The SEG in the outer region of the TPC (partition II) is larger due to the increased distance between the liquid-gas interface and the anode. In the near-wire region, the SEG is smaller. Because of the weaker position resolution, the SEG X-Y distribution does not exhibit the same pattern as shown in Fig. 12. The black circle is slightly larger than the TPC radius (i.e., 66.4 cm) because the single-electron gain selection accounts for the position resolution, as discussed in Sec. IV B.

bottom panel in Fig. 11 for P-I, which was propagated to the whole SR0. No REE evolution was observed in P-II; therefore, the correction factors in P-II were set to one.

These two time-dependent corrections for S2 signals, labeled as  $SEG_{\text{corr}}$  and  $EE_{\text{corr}}$ , helped restore background data near the ramping electrode events, representing 7.1% of the total exposure. The corrected S2 signal, cS2, after spatial and time-dependent corrections are applied, is computed as

$$cS2 = \frac{S2 \cdot \exp\left(\frac{\Delta t_{\text{diff}}}{\tau_{\text{EL}}(t)}\right)}{c(X, Y) \cdot SEG_{\text{corr}}(X, Y, t) \cdot EE_{\text{corr}}(X, Y, t)}. \quad (7)$$

## VI. SELECTION CRITERIA

This section describes the criteria applied to the nuclear recoil WIMP search and the low-energy ER analysis [5,9]. The aim is to select single-scatter events in the region of interest while rejecting unphysical events and improperly reconstructed events.

### A. Operating conditions of data acquisition

A series of selections based on the operational conditions during data acquisition have been used to remove data during certain time periods.

For most science data taking, the DAQ systems of the three detectors were synchronized [29]. Synchronization checks among the XENONnT detectors were conducted using a GPS clock signal (0.1 Hz) [48]. Initially, during the start of SR0, the GPS clock was not fully operational, resulting in the linked data-taking mode being unavailable for the three detectors for approximately 8% of the total data collection period. Any periods of linked data acquisition that might have exhibited synchronization loss were to be excluded; however, such instances did not occur during SR0.

If a digitizer's buffer is full, its board cannot accept further data from the photosensors, resulting in partially acquired events. The DAQ veto selection rejects these data acquisition periods, resulting in a 0.04% reduction of the live time in SR0.

The muon veto detector (MV) aims to detect muons and muon-induced backgrounds, particularly fast neutrons from muon spallation and electromagnetic or hadronic muon cascades. Whenever this happens, the TPC data acquisition is vetoed for 1 ms. This hardware trigger requires signals larger than 1 PE in at least 10 MV PMTs within a 300 ns time window. The tagging efficiency for backgrounds induced by muons crossing the water tank, or external muons with a shower in the water tank, is equal to 100% and 38%, respectively, as it was estimated in [49]. The muon veto criterion reduces these backgrounds by a factor of 2.8 with a 1% loss of live time.

The neutron veto, operating with pure water in SR0, aims to tag neutrons with one energy deposition in the TPC. These neutrons are detected by observing the Cherenkov light emitted when they are captured by a hydrogen atom. For the NR WIMP search, the NV issues a veto signal for each NV event with at least five PMT signals recorded and a total area of at least five PE [11]. A neutron tagging efficiency of  $(53 \pm 3)\%$  is estimated using neutrons from the  $^{241}\text{AmBe}$  source, in coincidence with 4.4 MeV gammas from deexcitation of  $^{12}\text{C}$ , which originate by the capture of  $\alpha$  particles on  $^9\text{Be}$ , recorded by the TPC [11]. This is slightly reduced to  $(50 \pm 3)\%$  due to the unlinked data-taking period. For details on the background modeling, see [8]. Motivated by the estimated characteristic neutron-capture time of  $(174 \pm 11) \mu\text{s}$ , all the S1 signals in a time window  $(-1, 249) \mu\text{s}$  around the center time of the neutron-veto event are vetoed [5].

Conversely, the ER search uses the coincidence of three NV PMTs as a trigger requirement. The lower threshold is acceptable as the veto window is reduced to a  $\pm 300$  ns window in which S1 signals of a TPC event are vetoed [9]. A factor of 8% reduction in the gamma-ray contribution from the decay of radionuclides in the detector material is estimated from science data.

The live time loss due to NV selection is 1.6% and 0.03% for the WIMP and low-energy ER analyses, respectively.

### B. Accidental coincidence suppression

Accidental coincidences (AC) arise from the random pairing of isolated S1 and S2 peaks. A few plausible origins may be fake S1 signals from pileup lone PMT hits, misclassified single electrons mistaken for S1 signals, and S2's from pileup few-electron signals arising from various sources.

A series of selections based on the temporal and spatial correlation of these events with previous large peaks are used to suppress AC-like events. Events occurring within one maximum drift time from an S1 (S2) signal larger than  $10^3$  PE ( $10^4$  PE) are vetoed. For a time difference  $\Delta t_{\text{prev}}$  larger than one maximum drift time, S2 peaks occurring too close to a triggering S2 peak are vetoed based on a quantity called “time shadow” defined as

$$S2_{\text{time shadow}} = S2_{\text{prev}} / \Delta t_{\text{prev}}. \quad (8)$$

A threshold of 0.038 PE/ns allows suppression of isolated S1 peaks while maintaining 96% signal acceptance. The spatial distance between previous large S2 signals and isolated S2's, described as a half-Cauchy distribution  $\rho(\sqrt{\Delta X^2 + \Delta Y^2})$  [26], is used to reduce the AC-like events due to delayed extracted electrons. The rejection region is a function of  $S2_{\text{time shadow}}$ , as shown in Fig. 14. This selection retains  $\sim 97\%$  signal acceptance.

The impact of a large S2 signal on the SE rate is significant, resulting in an increase in both the misclassification of S1 signals as SE (leading to isolated S1 signals) and the occurrence of SE pileup (leading to isolated S2 signals). AC-like (S1, S2) pairs are suppressed based on the number of peaks occurring in a 2 ms window before the S1 and within a radius of 6.7 cm from the S2 signal. The threshold of the number of peaks allowed is chosen to satisfy  $\sim 99\%$  signal acceptance.

To further mitigate AC-like events in the WIMP analysis, a gradient boosted decision tree (GBDT) algorithm [50] is employed. This algorithm is trained using simulated signal events to enhance its effectiveness. Five features are used in training: S2 rise time (see Sec. III A), the time interval in which 50% and 90% quantiles of the S2 peak are contained, the S2 peak area, and the observed Z position. The algorithm returns a metric, or score, for each event to be signal-like and AC-like. To avoid loss in the signal acceptance, two algorithms are used depending on whether the S2 area is smaller or larger than 2000 PE. The rejection thresholds for the GBDT scores, equal to 0.84 and 0.55, respectively, have been chosen to guarantee an acceptance of more than 95% in the region of interest.

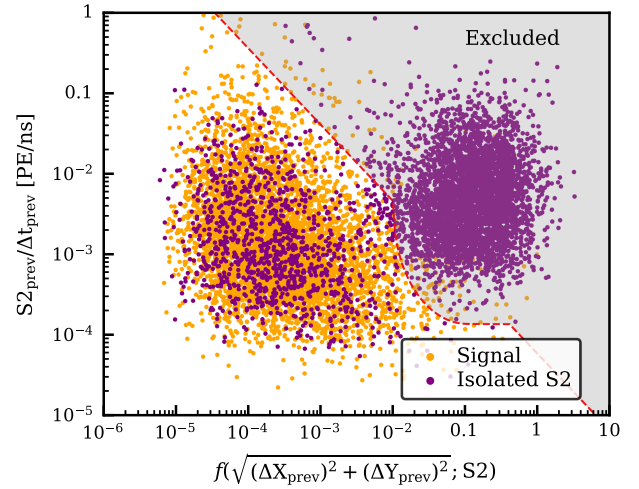


FIG. 14. S2 position shadow distribution. In orange are shown signal events from a benchmark simulation, whereas in purple is shown an isolated S2 population extracted from data. The red dashed line represents the rejection boundary. The time shadow quantity is shown as a function of the half-Cauchy distribution of position differences between an isolated S2 signals and its preceding S2 peak, with the X scale reflecting the peak's position reconstruction accuracy. The S2 signals of a true event and previous S2's have no positional correlation and accumulate in the left region. However, for isolated S2 signals, the opposite is true. This can be used to distinguish between signal and isolated peaks.

### C. Signal reconstruction requirements

Incorrectly reconstructed events, members of known background populations, and low-quality signals are removed by a set of requirements on the reconstructed signals.

- (i) Large deviations in the results of the different position reconstruction algorithms indicate a modeling error or an abnormal event. Data quality is improved by rejecting events with a position difference greater than the 99% quantile of position differences seen in high-quality calibration data (see Sec. II A). The quantile is a function of S2 area, because the position reconstruction performance varies with the S2 area.
- (ii) Events with S1's dominated by one PMT are suspicious. Typically, they are caused by a PMT malfunction, such as afterpulses or light emission [12]. At the top of the detector, events where a PMT contributes more than 6% plus an offset of four PE to the S1 are rejected. Events lower in the detector have more concentrated S1 hit patterns, so the rejection boundary is linearly increasing to 13% for events reconstructed at the cathode.
- (iii) Events with an S1 characterized by abnormal temporal widths are typically due to misidentified SE signals. They are excluded by special selection

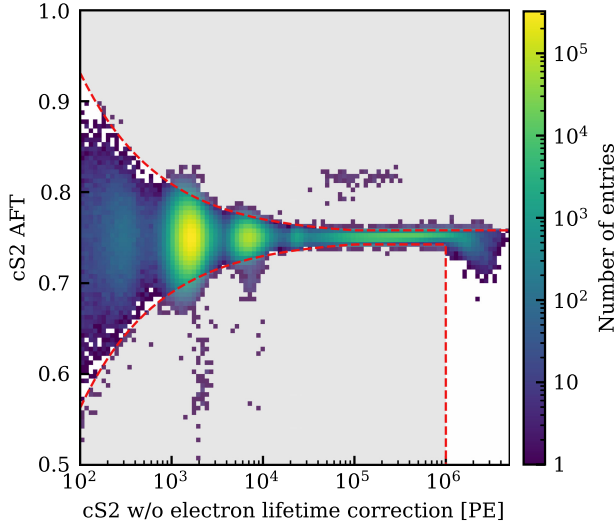


FIG. 15. Distribution of cS2 area fraction top vs cS2 signal area without electron lifetime correction as measured in  $^{241}\text{AmBe}$  and  $^{37}\text{Ar}$  calibration data. The dashed red line demarcates the selection criteria.

criteria based on the 50% and 90% quantiles of the S1 peak. The rejection regions are defined based on the 99% quantiles in the examined parameter spaces as a function of the signal size observed in high-quality calibration data.

- (iv) Events whose S2 is either a misidentified S1 or caused by gas phase interactions above the anode electrode are removed using the fraction of the S2 signals light collected by the top PMT array. Events with a corrected S2 light fraction in the top array outside the 0.5% and 99.5% quantiles, defined as a function of the corrected S2 area, are discarded. As before, the quantile lines are derived from a high-quality calibration data sample and are used as rejection limits up to  $10^5$  PE; above this, a constant extrapolation is used. To avoid unnecessary loss of signal acceptance, the lower boundary is removed for signals larger than  $10^6$  PE. The S2 top array light fraction is related to only the light transmission, so the selection is based on the S2 signal before the electron lifetime correction. The rejection criterion is shown in Fig. 15.
- (v) The consistency between the observed and expected S2 pattern intensity distribution on the top PMT array is quantified by a  $\chi^2$  goodness-of-fit test and outlier events are rejected. The expected light distribution is derived from a data-driven map built on a neural network fed with high-quality  $^{83\text{m}}\text{Kr}$  calibration data. The 99% quantile of the  $\chi^2$  distribution as a function of S2 area is used as the selection criterion. This selection mainly suppresses the pileup of delayed electron signals, double scatters, and misreconstructed events. Because of a loss of

accuracy in the data-driven map for large S2 areas, this criterion is limited for events with S2's smaller than  $3 \times 10^4$  PE.

- (vi) A naive Bayes classification method [51] is used to quantify whenever the S1 and S2 have the expected waveform shape. This machine-learning algorithm, based on a 50-sample waveform of the peaks and on a 50-sample quantile representation of peak waveforms, assigns each peak a score indicating the accuracy with which they were reconstructed. Events in the 99% quantile line in the parameter space of S1 (S2) score and S1 (S2) size are not further considered in the analyses. These selections effectively remove misclassified single electrons, gas events, unresolved double scatters, and afterpulse-contaminated S1's from the dataset.

#### D. Event requirements

A high quality of S1-S2 pairing is guaranteed by selection criteria developed by exploiting the correlation of event features and the position of the original interaction.

- (i) Events with anomalous S1 light pattern distributions, e.g., from unresolved multiple scatters or partially reconstructed events, can be rejected by comparing the S1 hit patterns with the expected patterns derived from optical MC simulations. The selection criteria are tuned to accept S1-S2 signal pairs from physical interactions in calibration control samples with a probability greater than 99%.
- (ii) Similarly, the correlation between the fraction of the S1 signal observed by the top array and the reconstructed event position is used to reject unphysical events. This quantity follows a binomial process: Each observed photon is seen by either the top or bottom PMT array, and the probability depends solely on the event's location and detector geometry. A well-motivated data quality criterion, based on the p value of the binomial test, is used to suppress accidental S1-S2 pairings and poorly reconstructed events.
- (iii) The ionization electron cloud, created by a particle interaction in liquid xenon, diffuses over time, which affects the features of the reconstructed S2's. The S2 width, or the time interval  $r_{50}$  in which the 50% quantile of the S2's area is contained, is correlated with the drift time  $\Delta t_{\text{drift}}$  of the event. Diffusion ensures a Gaussian distribution for the electron cloud, so this can be described [52] as

$$r_{50} = \sigma_{50} \sqrt{\frac{2D_L \cdot (\Delta t_{\text{drift}} - \Delta t_{\text{gate}})}{v_d^2}}, \quad (9)$$

where  $\sigma_{50} \approx 1.35$  is the conversion from Gaussian standard deviation to the 50th area range,  $D_L$  is the

field-dependent longitudinal diffusion coefficient, and  $v_d$  is the drift velocity. For the purpose of modeling solely the electron diffusion, the observed drift time must be corrected for the drift within the extraction field, from the gate to the liquid-gas interface,  $\Delta t_{\text{gate}}$ . The three parameters required to model the S2 width are drift field dependent and are determined from  $^{83\text{m}}\text{Kr}$  calibration data:  $D_L = (45.6 \pm 0.1) \text{ cm}^2 \text{ s}^{-1}$ ,  $v_d = (0.675 \pm 0.006) \text{ mm } \mu\text{s}^{-1}$ , and  $\Delta t_{\text{gate}} = (4.4 \pm 0.5) \text{ } \mu\text{s}$ . While the expected value of the S2 width of an event depends only on the drift time, the spread of the distribution of S2 width is highly dependent on the size of the S2 signal. Therefore, an S2 area-dependent selection based on the ratio between the observed width of an event and the width expected from a model, called the “normalized width”  $r_{50}^{\text{norm}}$ , is used to ensure correlation:

$$r_{50}^{\text{norm}}(\Delta t_{\text{drift}}) = \frac{r_{50}(\Delta t_{\text{drift}})^2 - (r_{50}^{\text{SE}})^2}{r_{50}^{\text{model}}(\Delta t_{\text{drift}})^2}. \quad (10)$$

The quantity  $r_{50}^{\text{SE}} \sim 375 \text{ ns}$  is introduced to correct the width model for a small number of electrons in the electron cloud and is calculated from the observed single-electron population. For events in the vicinity of the transverse wires, the observed S2 widths are larger than in the rest of the TPC due to longer drift times caused by the distortion of field lines induced by the wires and the resulting lower drift field below the gate. Thus, the selection follows a different definition for events reconstructed within 4.45 cm of the perpendicular wires. In Fig. 16, the boundaries of the cut in the region far from the wires are shown. They are defined as the 1st and 99th percentiles of the distributions of signal-like simulated data for S2 signal less than  $10^4$  PE and otherwise on  $^{220}\text{Rn}$  data. The broadening of the distribution for small S2 signal sizes is caused by binomial fluctuations in the number of electrons contributing to the signal.

In the near wire region, the 1st and 5th percentiles in the  $(\text{S2}, r_{50}^{\text{norm}}(\Delta t_{\text{drift}}))$  parameter space of the observed data are used to define the lower boundary of the cut for the low-energy ER and WIMP searches, respectively. The different boundary conditions were motivated by varying AC contributions for the two analyses. For the low-energy ER analysis, we preferred higher signal acceptance, whereas for the WIMP search, we chose to optimize AC background suppression. In addition, the difference between the  $r_{50}(\Delta t_{\text{drift}})$  and  $r_{50}^{\text{model}}$  as a function of the distance from the perpendicular wires ( $\Delta x_{\text{wire}}$ ) is used to discriminate anomalous events.

The upper boundary in this region is defined using a dedicated model that accounts for distortions in the

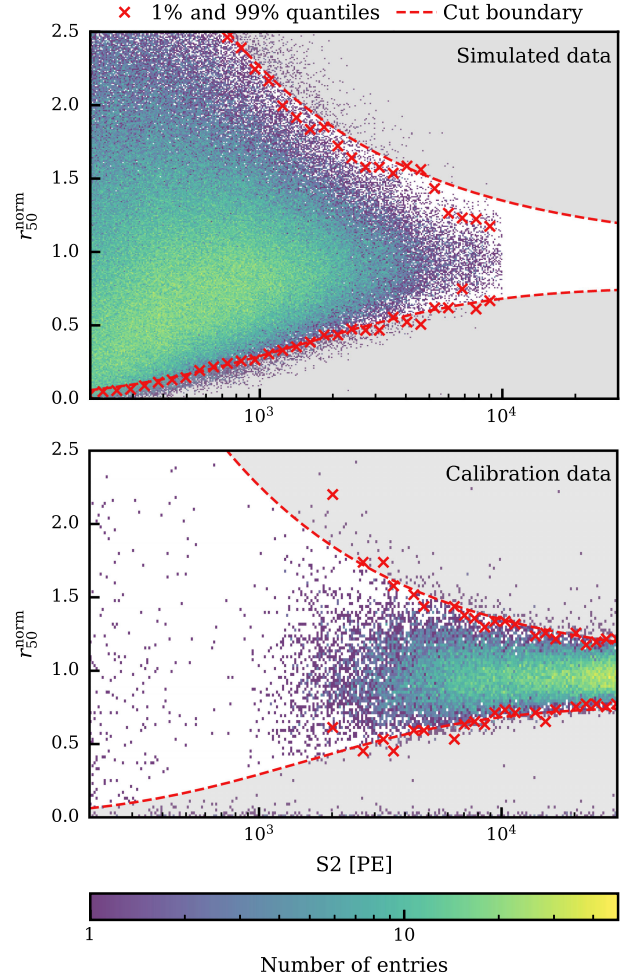


FIG. 16. Distribution of the S2 width parameter  $r_{50}^{\text{norm}}$  as a function of S2 signal area for simulated (top) and  $^{220}\text{Rn}$  calibration (bottom) data for events reconstructed far from the perpendicular wires. Red crosses mark the 1% and 99% quantiles, and the dashed line shows the selection criterion definition for the far-wire region.

electric field near the wires, which elongate the S2 widths. To address these distortions, the boundary is defined in a rescaled space where the rescaling factors are the S2 width spread (for the y axis) and the position resolution (for the x axis). The rescaled boundary consists of three components: a constant region, a linear transition, and a circular segment. The constant value and its transition to the linear region depend on the S2 width spread and position resolution and are estimated using the upper boundary from simulations. The slope of the linear segment is fixed using the 98th percentile of  $^{83\text{m}}\text{Kr}$  calibration data. The transition between the linear and circular segments occurs at a specific point determined by the slope of the linear region. The circular segment is described by the equation  $y_{\text{circle}} = y_c + \sqrt{1 - |\Delta x_{\text{wire}}|^2}$ , where  $y_c$  represents the center of the circle in the rescaled space.

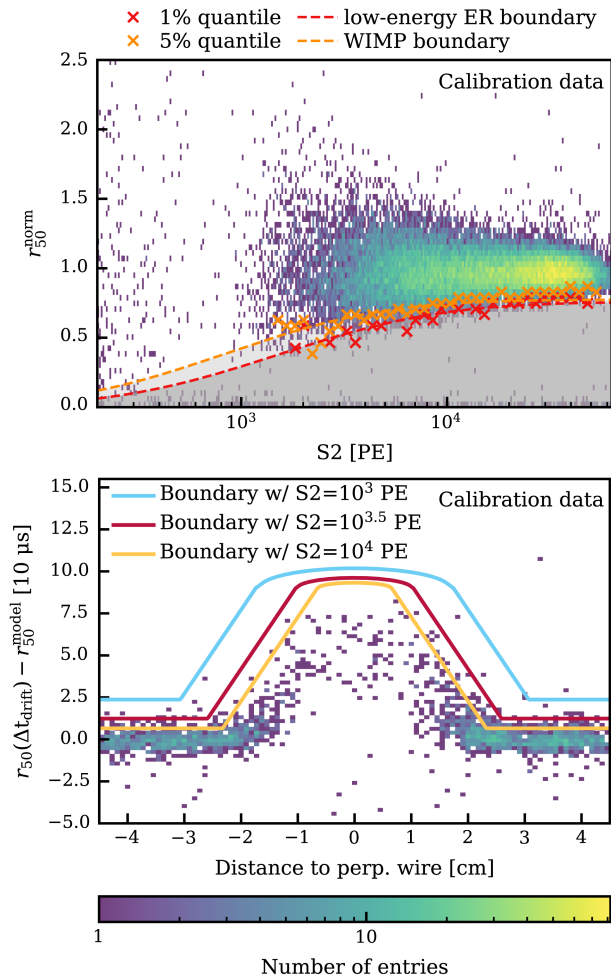


FIG. 17. Distribution of the measured S2 width parameter  $r_{50}^{\text{norm}}$  as a function of S2 signal area for  $^{220}\text{Rn}$  calibration data reconstructed in the near-wire region. The orange and red crosses show the 1% and 5% quantiles of the data, respectively, which are used to define the selection criteria used in the main XENONnT analysis, as depicted by the legend (top). Difference between expected and measured S2 width parameter  $r_{50}$  as a function of the distance of the observed position to the perpendicular wires for  $^{220}\text{Rn}$  calibration data. Three lines are shown: the S2 width cut upper boundaries for near-wire regions for different S2 signal areas (bottom).

Dependence on S2 signal area and  $\Delta t_{\text{drift}}$  is incorporated into the rescaling factors to build the model. Larger S2 signal areas reduce the S2 width spread and position resolution, leading to narrower boundaries. Conversely, longer drift times increase the S2 width spread, resulting in broader distributions. The selection definition is portrayed in Fig. 17.

### E. Single-scatter requirements

Given the small expected scattering cross section of dark matter particles and the small mean free path of photons and electrons in the energy range of interest, the signals

searched (WIMP and other low-energy ER signals) are expected to have only single energy depositions in the TPC. Identifying multiple-scatter events is a powerful discriminator between signal candidates and certain backgrounds. For example, radiogenic neutrons have a probability larger than 80% to induce multisite events.

- (i) Events with alternative S1's recorded in the waveform that could also form a valid interaction with the primary S2 are rejected. Whether the alternative S1 and the main S2 do not constitute a valid interaction is based on the S2 width, S1 AFT, and the light distribution of the alternative S1. S1 signals with abnormally high contributions of a single PMT are not considered for pairing with the S2. This selection targets not only multienergy deposition events with delayed coincidence, but also those with ambiguous identification of the primary S1.
- (ii) Events with an additional S2 in the waveform are considered multiple scatter if the signal ratio with the main S2 is larger than a few percent. The threshold is based on high-quality calibration data and is defined as a function of the primary S2 area, as shown in Fig. 18. Artifact are valid single-scatter events.

### F. Fiducial volume

The rejection of the periphery of the detector is the most robust selection against poorly reconstructed events and several backgrounds.

The fiducial volume (FV) optimization uses the background components' expected  $(R^2, z)$  distributions,

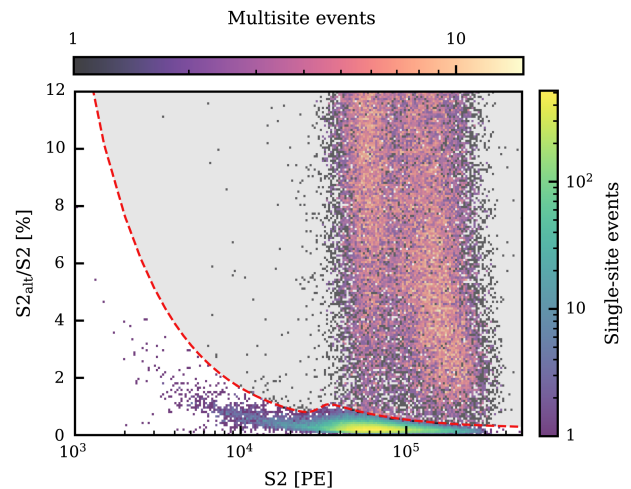


FIG. 18. Distribution of  $S2_{\text{alt}}/S2$  as a function of S2 area for  $^{220}\text{Rn}$  calibration data. The dashed line defines the adopted S2 single-scatter selection definition and divides the single-site and the multisite populations. Approaching high S2 signals, the selection definition is relaxed due to the nonoptimal STRAXEN performance for high-energy peak splitting and merging. The two populations in the multisite events are due to the gamma transitions followed by the beta decay of  $^{212}\text{Pb}$ , daughter of  $^{220}\text{Rn}$ .

excluding regions where detector understanding is limited. The optimization region considered falls below 100 PE S1 and loosely within either the NR or ER bands. Specifically, it is between the 1st percentile of a 50 GeV/ $c^2$  WIMP in cS2 and the 99th percentile of the ER background (or a low-energy ER signal) in cS2. ER background is mostly from homogeneously distributed  $^{214}\text{Pb}$   $\beta$  decays and inhomogeneously distributed  $\gamma$  emission from detector materials. Their position distribution is modeled using unblinded background events with reconstructed energy between 20 and 40 keV. The AC model is data driven, constructed using unpaired S1's and S2's from the physics data, randomly paired to build high-statistics artificial data, and validated against calibration data. The spatial distribution of ACs is approximately constant over the detector volume and, thus, does not substantially impact the fiducial volume optimization. Events near the TPC wall, originating, e.g., from the  $^{222}\text{Rn}$  progeny plated out on the inner surface of the PTFE panel, tend to lose a fraction of their charge in the PTFE panels [8]. This leads to events characterized by a low charge-to-light ratio, which may be inaccurately reconstructed further inside the TPC radius. These events are modeled using sidebands of blinded WIMP search data [8]. NR events are expected from radiogenic neutrons produced through spontaneous fission or  $(\alpha, n)$  reactions in detector materials and from coherent elastic neutrino-nucleus scattering from neutrinos [17]. The spatial distribution of the latter is uniform; therefore, it is not considered during the optimization of the fiducial volume. For the background of radiogenic neutrons, the neutron yield is simulated using Geant4, and it is adjusted to match the expected number of background events as forecasted by the SOURCES-4A simulation package [53,54]. The derived position distribution has been propagated to determine the choice of fiducial volume.

To exclude misreconstructed events from the gas volume, events reconstructed with  $Z < -6$  cm are excluded. Additionally, TPC regions where the difference between simulation and the data-driven electric field is larger than 10% are not further considered. These are well confined at a high radius and close to the cathode and gate electrodes. The top right corner is also removed due to the high ER background and relatively high electric field variation in that region. Lastly, the maximum radius is set as 63 cm for the low-energy ER analysis and 61.35 cm for the WIMP search to reject the bulk of surface background events, as shown by the solid and dashed blue lines in Fig. 19, respectively.

The xenon mass contained in the FV is derived from geometrical considerations, assuming a liquid xenon density of  $(2.862 \pm 0.003)$  t/ $\text{m}^3$  [55], considering the presence of S2-insensitive mass (see [14] for additional information) and given the best knowledge of the drift field as well as the resolution of the position reconstruction. The field distortion correction defined for SR0 does not include the effect of a small charge-insensitive volume near the cathode and at the periphery of the TPC, which

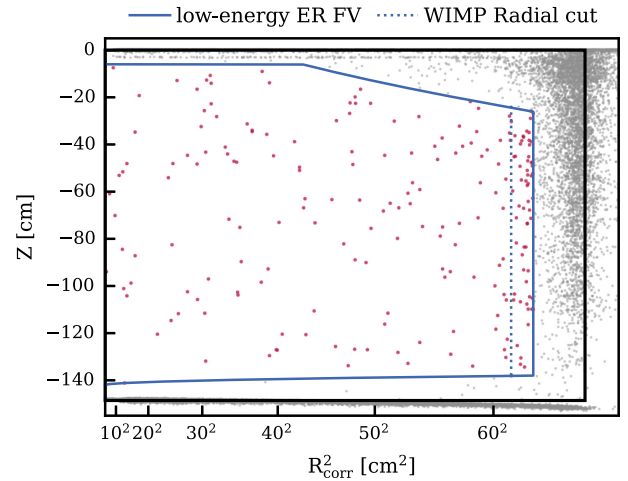


FIG. 19. Observed data in  $(R^2, Z)$  space of the SR0 WIMP search. The red dots are the events that have been reconstructed in the fiducial volumes. The solid black box demarcates the TPC volume, whereas the solid and dotted blue lines show the adopted fiducialization for the main XENONnT SR0 analyses [5,9].

effectively reduces the maximum radius of the TPC. We do consider the effect that this has on the mass contained in the fiducial volume. The FVs contain  $(4.37 \pm 0.14)$  t and  $(4.18 \pm 0.13)$  t of liquid xenon for the low-energy ER analysis and WIMP search, respectively. The uncertainties include the position reconstruction resolution (0.1%) and the dimension of the charge insensitive mass based on electric field simulations (3%).

### G. Signal acceptances

Figure 20 shows the cumulative signal acceptances of the described categories of selection criteria as a function of the reconstructed energy and the uncorrected S1 and S2 signal sizes. The acceptance of each selection, namely, the signal events that pass through the selection, is estimated by using the *N-1 method*, namely, evaluating the Nth selection acceptance after applying the previous N-1 criteria. The uncertainties in the acceptances were inferred using the Clopper-Pearson method [56]. The acceptances were estimated using  $^{220}\text{Rn}$  and  $^{37}\text{Ar}$  calibration data in a  $\sim 4$  tonne fiducial volume, equivalent to  $R < 60.73$  cm and  $Z \in [-13.6; -134.2]$  cm, in order to reduce contamination from surface events observed at higher rates during calibration. The acceptances derived within this region are assumed to remain valid up to the full fiducial volume limit. This assumption is supported by an evaluation of the cut acceptance radii profile, showing no significant variation beyond the calibrated region. Complementary, synthetic signal-like events from the waveform simulation were used to establish the acceptances, e.g., for the accidental coincidence and S2 width criteria. Whenever a significant correlation is observed between two or more selections, these are grouped, and their cumulative acceptance is

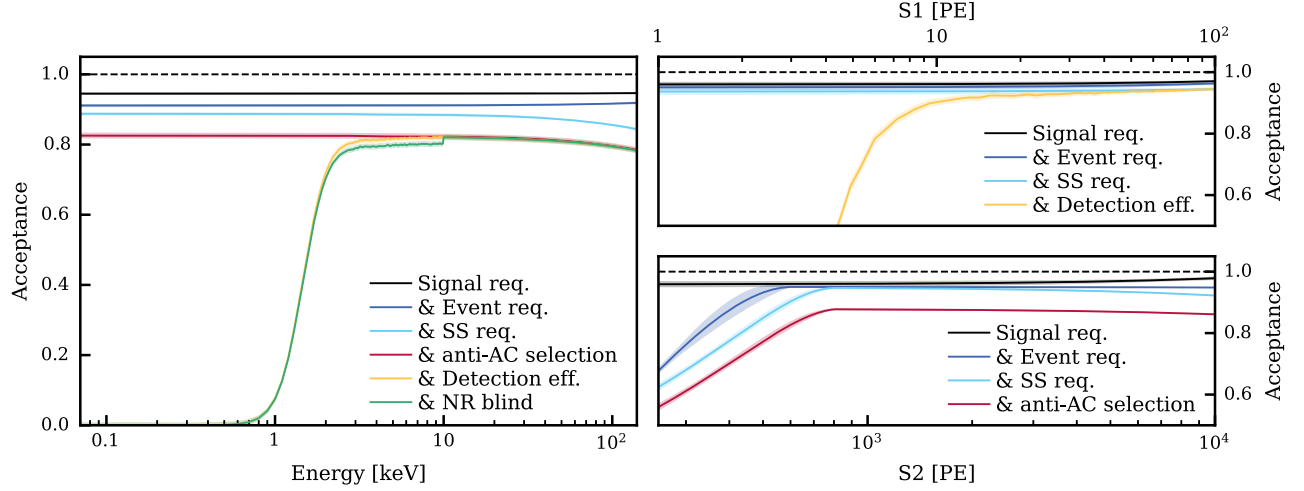


FIG. 20. Evolution of the acceptance by incrementally applying the selection criteria categories described in the text as a function of reconstructed energy for low-energy ER analysis (left) and uncorrected S1 and S2 signal areas for WIMP search (right). The shade bands represent the acceptance uncertainty. The 10 keV discontinuity in total acceptance as a function reconstructed energy marks the WIMP-blinded region, relevant only for low-energy ER analysis. The total acceptance is also shown after considering the reconstruction efficiencies.

estimated. This is the case for S2 width and GBDT anti-AC criterion. Selections dealing with properties unrelated to the event are deemed exposure reduction cuts, e.g., fiducialization or selections based on operational conditions. The smooth curves in Fig. 20 are determined by fitting polynomial functions to the data points. The uncertainty bands account for the uncertainty from the fitting procedure.

In the S1 signal space, the selection criteria have a similar impact with an average acceptance equal to  $(98.1 \pm 0.9)\%$ . In the S2 signal space, the acceptance is primarily influenced by the anti-AC requirements and the event quality criteria, particularly the S2 width selection criterion. The discontinuity at 10 keV in the total acceptance as a function of the reconstructed energy is caused by the WIMP blinded region, and it is relevant only for low-energy ER analysis. After including the reconstruction efficiencies discussed in Sec. III C, the total acceptances are propagated into the statistical inference for dark matter and low-energy ER searches.

## VII. ENERGY RECONSTRUCTION AND RESOLUTION

The energy deposited in an ER interaction ( $E_{\text{ER}}$ ), which is converted into scintillation photons  $n_{\text{ph}}$  and ionization electrons  $n_e$ , can be expressed as a function of the reconstructed cS1 and cS2 signals by introducing the photon detection efficiency  $g_1$ , also known as photon gain, and electron gain  $g_2$ :

$$E_{\text{ER}} = (n_{\text{ph}} + n_e) \cdot W = \left( \frac{\text{cS1}}{g_1} + \frac{\text{cS2}}{g_2} \right) \cdot W, \quad (11)$$

where  $W = (13.7 \pm 0.2)$  eV/quantum [57] represents the mean energy required to create either scintillation or ionization quanta. The  $g_1$  and  $g_2$  factors are detector-dependent parameters assessed using monoenergetic peaks, including  $^{37}\text{Ar}$ ,  $^{83\text{m}}\text{Kr}$ ,  $^{129\text{m}}\text{Xe}$ , and  $^{131\text{m}}\text{Xe}$ . Higher-energy lines of  $^{60}\text{Co}$ ,  $^{40}\text{K}$ ,  $^{214}\text{Bi}$ ,  $^{12}\text{C}$ , and  $^2\text{H}$  are excluded from the fit due to missing high-energy optimizations of the signal reconstruction and correction but still reported for completeness. The selection criteria outlined earlier are applied to all data, with the exception of the  $^{83\text{m}}\text{Kr}$  calibration, which uses dedicated topology-based cuts. The measurement for each source of the mean charge yields ( $\text{CY} = \text{cS2}/E$ ) and light yields ( $\text{LY} = \text{cS1}/E$ ) allows for the reconstruction of a linear energy response of both S1 and S2 signals by rewriting Eq. (11) to

$$\text{CY} = -\frac{g_2}{g_1} \cdot \text{LY} + \frac{g_2}{W}. \quad (12)$$

The anticorrelation of light and charge signals outlined in Eq. (11) leads to monoenergetic lines appearing as rotated ellipses when plotting cS1 against cS2, as depicted in Fig. 21 for the full energy range of the merged calibration and blinded data. Rotated two-dimensional Gaussian functions are used to fit each monoenergetic ellipse and extract its corresponding LY and CY. This method has been adapted to each monoenergetic source as described in the following.

- (i) For the K-shell  $^{37}\text{Ar}$  peak at 2.82 keV, being close to the S1 detection efficiency introduced in Sec. III C, it is necessary to perform the fit in the uncorrected S1 and cS2 parameter space. The detection volume is segmented in different voxels,

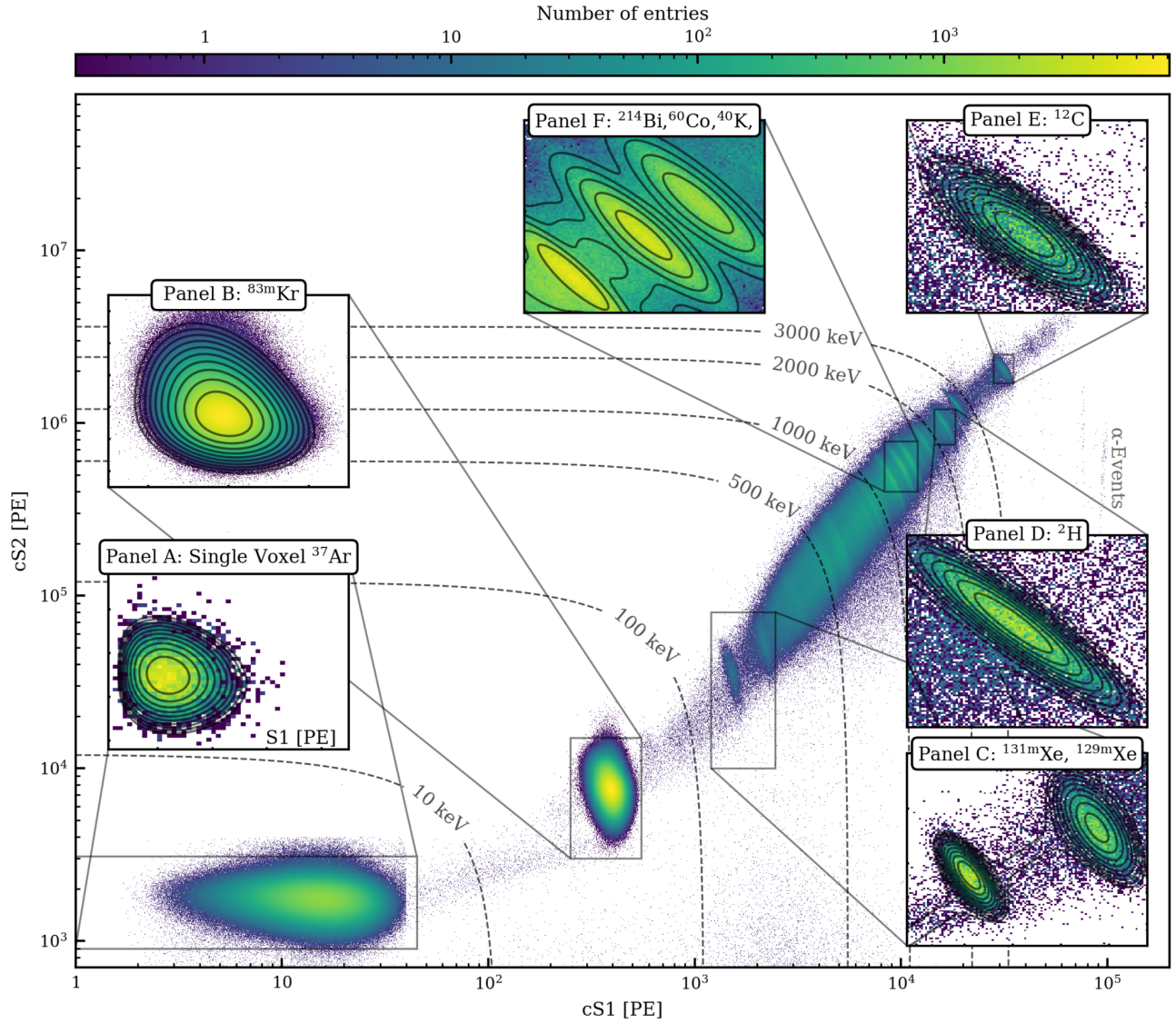


FIG. 21. Two-dimensional histogram in  $cS1$  and  $cS2$  space covering most of the XENONnT energy range. The monoenergetic lines used in to extract the  $g_1$  and  $g_2$  parameters are highlighted in subplots. The displayed data are a combination of multiple calibration datasets ( $^{37}\text{Ar}$ ,  $^{83\text{m}}\text{Kr}$ , and  $^{241}\text{AmBe}$ ) as well as background data. The  $^{37}\text{Ar}$  subplot displays the fit in a single voxel using the  $S1$  and  $cS2$  space. Events of the activated xenon lines  $^{131\text{m}}\text{Xe}$  and  $^{129\text{m}}\text{Xe}$  as well as  $^{12}\text{C}$  and  $^2\text{H}$  events are present in  $^{241}\text{AmBe}$  calibration data.  $^{60}\text{Co}$ ,  $^{214}\text{Bi}$ , and  $^{40}\text{K}$  can be found in background,  $^{83\text{m}}\text{Kr}$  and  $^{241}\text{AmBe}$  calibration data but only background and  $^{83\text{m}}\text{Kr}$  calibration data are used for the corresponding fit.

and the  $L_c(\mathbf{R}, \phi, Z)$  correction shown in Eq. (4), evaluated in each voxel barycenter, was manually applied to the  $S1$  mean obtained. The  $S1$  signal is modeled with a skew-Gaussian distribution, which has proven to be a more suitable model for  $\mathcal{O}(1)$  keV ERs [20], convolved with the data-driven estimation of the  $S1$  detection efficiency. For  $cS2$ , a normal distribution is considered. An example of 2D fit in a single voxel with the projections is shown in Fig. 21 panel A. The average LY and CY over all the voxels,  $\langle \text{LY} \rangle = (5.3325 \pm 0.0014)$  PE/keV and  $\langle \text{CY} \rangle = (320.4 \pm 0.3)$  PE/keV, are used to derive the  $g_1$  and  $g_2$  parameters.

- (ii) The  $^{83\text{m}}\text{Kr}$  peak, shown in Fig. 21 panel B, exhibits a tail toward larger  $cS2$ , most likely induced by nonperfect signal correction of field inhomogeneities. This artifact is also present in the other monoenergetic lines but has a negligible impact on the LY/CY measurement. A skew-Gaussian in  $cS2$  is used to model the observed tail.
- (iii) Unlike the former two monoenergetic lines that come from dedicated calibrations, the  $^{129\text{m}}\text{Xe}$  and  $^{131\text{m}}\text{Xe}$  lines are present in the background data after a neutron calibration. As depicted in Fig. 21 panel C, they stand on top of a continuous background band from Compton scatter and  $\beta$  decay. Therefore,

a two-dimensional function featuring a linear profile along the cS1 axis, a Gaussian profile along the cS2 axis, and a rotation angle in the plane are incorporated into the rotated 2D Gaussian to improve the fit.

- (iv) Several high-energy gamma lines (above 300 keV), either originating from the radiogenic background of the detector materials or induced during  $^{241}\text{AmBe}$  calibration, serve as additional reference lines. During  $^{241}\text{AmBe}$  calibration, alpha capture on  $^9\text{Be}$  creates a compound nucleus,  $^{13}\text{C}^*$ , which rapidly decays by emitting a neutron. This process can lead to an excited state of  $^{12}\text{C}$ , emitting a 4.4 MeV gamma. The neutron can also be captured by hydrogen in the water tank surrounding the TPC, leading to the emission of a 2.2 MeV gamma. Such a high-energy gamma can reach the sensitive volume of the TPC as shown in Fig. 21 panels D and E. Additionally, radiogenic gamma lines from  $^{60}\text{Co}$  with energies of 1173.2 and 1332.5 keV, and from  $^{40}\text{K}$  at 1460.8 keV, originate from the detector materials and can be seen in background data [Fig. 21, panel F]. These high-energy gamma lines are fitted with rotated 2D Gaussian functions, taking into account continuous background contribution from Compton scattering and beta decay. However, these lines are not included in the final  $g_1/g_2$  fit, as stated previously.

Before computing the gain parameters  $g_1$  and  $g_2$ , the measured LY and CY values are corrected for the energy-dependent peak reconstruction bias introduced in Sec. III D. This correction is applied only to the LY/CY measurement and not directly to the cS1/cS2 value, which results in a biased energy scale. To minimize this bias in the low-energy region, the peak reconstruction bias correction is rescaled to have zero bias for the  $^{37}\text{Ar}$  line. The observed energy bias is characterized and incorporated into the inference as discussed later. A systematic error of 3.2% on the CY is used to account for the average distance between the best-fit prediction using the four low-energy lines and the high-energy lines. Figure 22 shows the relation between measured CY and LY. Factors  $g_1$  and  $g_2$  are extracted using a linear fit following Eq. (12). The parameters extracted from the fit that allows us to build our ER energy scale are  $g_1 = (0.151 \pm 0.001)$  PE/ph and  $g_2 = (16.5 \pm 0.6)$  PE/e $^-$ .

The reconstructed energy of monoenergetic lines is fitted with a free skew-Gaussian function and a free linear background to model the detector's energy resolution. The skew-Gaussian function is defined as

$$f_{\text{skew}} = \frac{1}{\omega\sqrt{2\pi}} e^{-\frac{(E-\xi)^2}{2\omega^2}} \left[ 1 + \text{erf}\left(\frac{\alpha(x-\xi)}{\sqrt{2}\omega}\right) \right], \quad (13)$$

where  $\omega$  represents the width of the distribution,  $\xi$  is the location parameter (peak position), and  $\alpha$  characterizes

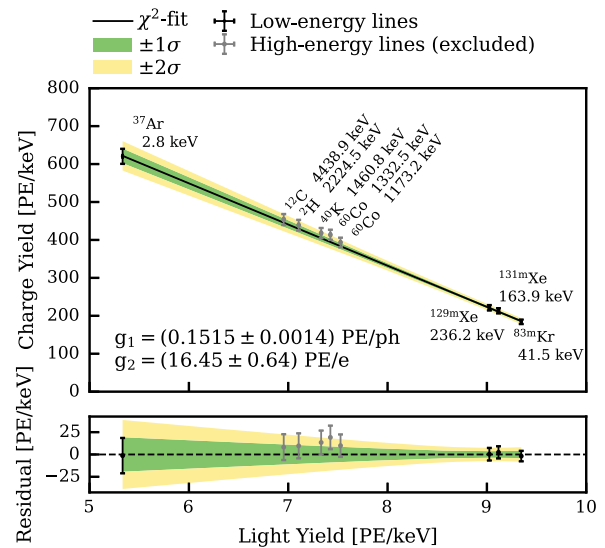


FIG. 22. Anticorrelation between the measured light yield and charge yield using monoenergetic lines. The black solid line represents the best linear fit to the data obtained from  $^{37}\text{Ar}$ ,  $^{83\text{m}}\text{Kr}$ ,  $^{129\text{m}}\text{Xe}$ , and  $^{131\text{m}}\text{Xe}$  low-energy lines. Data points derived from high-energy lines, not included in the fit, are displayed as gray markers. Despite not being used for the fitting process, these high-energy points remain consistent with the fitted model within their uncertainties.

the skewness of the distribution. From these parameters, the skew mean ( $\mu_{\text{skew}}$ ) and standard deviation ( $\sigma_{\text{skew}}$ ) are computed as follows:

$$\mu_{\text{skew}} = \xi + \omega \sqrt{\frac{2}{\pi}} \cdot \frac{\alpha}{\sqrt{1 + \alpha^2}}, \quad (14)$$

$$\sigma_{\text{skew}} = \omega \sqrt{1 - \frac{2\alpha^2}{\pi(1 + \alpha^2)^2}}. \quad (15)$$

This model better describes the mismodeling and imperfect signal correction of low-energy lines mentioned earlier. The top left panel in Fig. 23 shows the measured energy resolution ( $\sigma/\mu$ ) for the four low-energy lines used in the  $g_1/g_2$  fit, along with the empirical model fitted to these data points. The top right and bottom right panels display the width and skewness parameters, respectively, each annotated with their corresponding fitted values used to model the energy resolution. The skew-Gaussian model transitions to a regular Gaussian distribution for high-energy lines as the skewness converges to zero. The relative energy bias, shown in the bottom left panel in Fig. 23, is characterized using an empirical function in the reconstructed energy space and propagated into the analyses by reshaping the expected energy spectra. Additionally, the dominant KK-capture peak from  $^{124}\text{Xe}$   $2\nu\text{ECEC}$  decay at 64.3 keV [18] is shown as a cross-check of the energy reconstruction. The significant decrease in the background

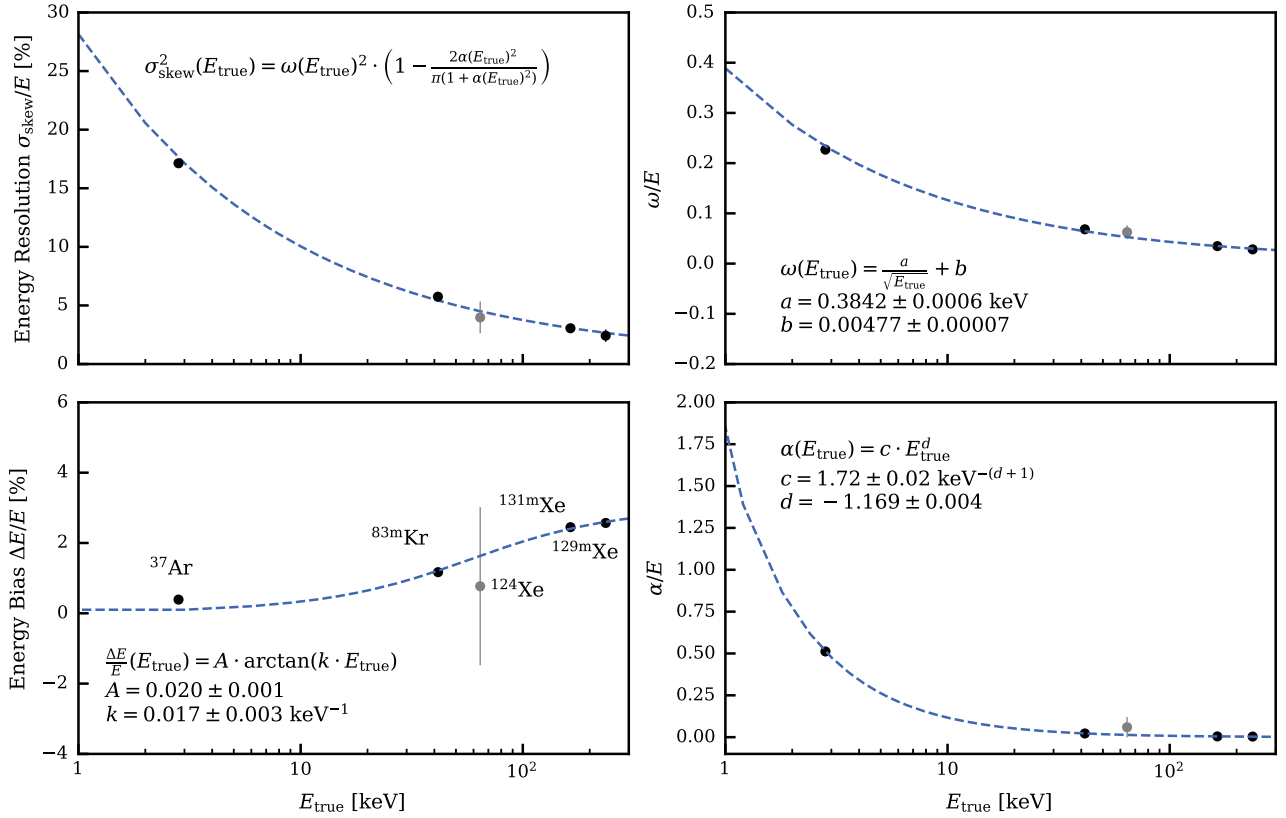


FIG. 23. The top left panel shows the measured energy resolution ( $\sigma/\mu$ ) from the low-energy lines used in the  $g_1/g_2$  fit (cf. Fig. 22). An empirical model, specifically tailored for the skew-Gaussian fitting method, characterizes the energy resolution, which depends on the width ( $\omega$ ) and skewness ( $\alpha$ ) parameter measurements. These parameters and their corresponding fits are displayed in the top right and bottom right panels, respectively, with the fitted parameter values annotated. The bottom left panel illustrates the relative energy bias, modeled with an empirical function, and its fitted parameters. The gray point (not included in the fits) shows the dominant KK-capture peak from <sup>124</sup>Xe  $2\nu$ ECEC decay, which was recently observed for the first time in the XENONIT experiment [18]. The energy resolution and the relative energy bias models are propagated to the main analyses by reshaping the expected energy spectra.

level makes this peak distinctly prominent, thereby rendering it particularly suitable for cross-checking the accuracy of the energy reconstruction process.

### VIII. CONCLUSION AND OUTLOOK

This paper presents the data analysis techniques employed for the WIMPs [5] and low-energy electronic recoil [24] searches during the first XENONnT science run. It details the processes of signal reconstruction and correction, event building, selection criteria, and energy estimation. The majority of the methodologies outlined are applicable to ongoing and forthcoming searches for WIMP, alternative dark matter hypotheses, and various low-background investigations.

Throughout the entire science run, the detector functioned under consistent conditions. The TPC photosensors exhibited stability and reliability in their response throughout the commissioning phase and first science run. A mere 3% of the PMTs were deemed nonoperational, corresponding to a failure rate of approximately a factor of 5 lower compared to XENONIT [26]. The light

and charge yield responses were stable throughout the entire science data taking, with fluctuation smaller than 1% and 1.9%, respectively. The improvement in the xenon purification allows us to reach unprecedented low concentrations of electronegative contaminants, thanks to which our electron lifetime was constantly above 10 ms. This is a factor 10 improvement with respect to XENONIT [26].

Regular calibrations using an <sup>83m</sup>Kr internal source were employed to assess the TPC's response and to calculate signal corrections. These corrections accounted for detector artifacts, such as distortions in the electric drift field and spatial inhomogeneity in detecting and reconstructing S1 and S2 signals. Additionally, internal sources of <sup>220</sup>Rn and <sup>37</sup>Ar were utilized to characterize the electronic recoil response. An external source of <sup>241</sup>AmBe was employed to assess the TPC response to nuclear recoil events and to evaluate the detection efficiency of the neutron veto [11]. For additional information regarding the characterization of the ER and NR detector responses, we recommend that readers consult [8].

A novel data processing software has been developed for the new XENONnT triggerless data taking [29]. Its performance is optimized based on full-chain waveform simulation, thanks to which the peak finding efficiencies, peak reconstruction, and event reconstruction biases are also estimated. Improved MC optical simulation of the TPC is employed to tune position reconstruction algorithms, and detailed electric field simulation is used to improve the homogeneity of the drift field and the understanding of the ionization signal [14]. The selection criteria resemble those used in XENON1T [26], with the addition of new criteria based on machine-learning techniques that have further enhanced the data quality. The more advanced analysis with respect to its predecessor, together with the hardware improvements for the background reduction (e.g., radon removal system), has made possible the measurement of the lowest background below 30 keV for a dark matter detector, equivalent to  $(15.8 \pm 1.3)$  events/(tonne · year · keV) consisting of a factor 5 reduction concerning XENON1T [24].

The anticorrelation between charge and light yields has been confirmed for energy depositions ranging from a few keV to the MeV scale. The calibration of the energy scale was achieved by utilizing the  $g_1 = (0.151 \pm 0.001)$  PE/ph and  $g_2 = (16.5 \pm 0.6)$  PE/e<sup>-</sup> detector parameters and by integrating both direct and proportional scintillation signals. The resulting energy resolution was found to be on par with XENON1T [33].

Although the foundational elements of the XENONnT analysis pipeline are well established, ongoing efforts are dedicated to enhancing it to improve detector performance further and deepen our understanding of its response. We are working toward understanding the origin of accidental coincidence backgrounds and exploring methods for their further reduction. Additionally, new calibration sources (e.g., <sup>232</sup>Th and YBe [58]) have been investigated to enhance the characterization of the detector's ER and NR responses. On the hardware front, ongoing improvements to the subsystem aim to increase xenon purity, which will benefit subsequent analyses. Lastly, the simulation framework is being refactored to adopt a more modular approach and to improve the physical description of the detector, such as electron diffusion below the perpendicular

wires. XENONnT is actively collecting new data, and advancements in hardware have significantly boosted its performance. The physics reach of XENONnT is broad, encompassing a variety of novel and compelling analyses currently in progress.

## ACKNOWLEDGMENTS

We gratefully acknowledge support from the National Science Foundation, Swiss National Science Foundation, German Ministry for Education and Research, Max Planck Gesellschaft, Deutsche Forschungsgemeinschaft, Helmholtz Association, Dutch Research Council (NWO), Fundacao para a Ciencia e Tecnologia, Weizmann Institute of Science, Binational Science Foundation, Région des Pays de la Loire, Knut and Alice Wallenberg Foundation, Kavli Foundation, JSPS Kakenhi and JST FOREST Program ERAN in Japan, Tsinghua University Initiative Scientific Research Program, DIM-ACAV+ Région Ile-de-France, and Istituto Nazionale di Fisica Nucleare. This project has received funding or support from the European Union's Horizon 2020 research and innovation program under the Marie Skłodowska-Curie Grant Agreement No. 860881-HIDDeN. We gratefully acknowledge support for providing computing and data-processing resources of the Open Science Pool and the European Grid Initiative, at the following computing centers: the CNRS/IN2P3 (Lyon, France), the Dutch national e-infrastructure with the support of SURF Cooperative, the Nikhef Data-Processing Facility (Amsterdam, Netherlands), the INFN-CNAF (Bologna, Italy), the San Diego Supercomputer Center (San Diego, USA) and the Enrico Fermi Institute (Chicago, USA). We acknowledge the support of the Research Computing Center (RCC) at The University of Chicago for providing computing resources for data analysis. We thank the INFN Laboratori Nazionali del Gran Sasso for hosting and supporting the XENON project.

## DATA AVAILABILITY

The data that support the findings of this article are not publicly available. The data are available from the authors upon reasonable request.

- 
- [1] G. Bertone, D. Hooper, and J. Silk, Particle dark matter: Evidence, candidates and constraints, *Phys. Rep.* **405**, 279 (2005).  
 [2] L. Roszkowski, E. M. Sessolo, and S. Trojanowski, WIMP dark matter candidates and searches—current status and future prospects, *Rep. Prog. Phys.* **81**, 066201 (2018).  
 [3] D. J. E. Marsh, Axion cosmology, *Phys. Rep.* **643**, 1 (2016).

- [4] M. Pospelov, A. Ritz, and M. Voloshin, Bosonic super-WIMPs as keV-scale dark matter, *Phys. Rev. D* **78**, 115012 (2008).  
 [5] E. Aprile *et al.* (XENON Collaboration), First dark matter search with nuclear recoils from the XENONnT experiment, *Phys. Rev. Lett.* **131**, 041003 (2023).

- [6] Y. Meng *et al.* (PandaX-4T Collaboration), Dark matter search results from the PandaX-4T commissioning run, *Phys. Rev. Lett.* **127**, 261802 (2021).
- [7] J. Aalbers *et al.*, First dark matter search results from the LUX-ZEPLIN (LZ) experiment, *Phys. Rev. Lett.* **131**, 041002 (2023).
- [8] E. Aprile *et al.* (XENON Collaboration), XENONnT WIMP Search: Signal & Background Modeling and Statistical Inference (to be published).
- [9] E. Aprile *et al.* (XENON Collaboration), Search for new physics in electronic recoil data from XENONnT, *Phys. Rev. Lett.* **129**, 161805 (2022).
- [10] E. Aprile *et al.* (XENON Collaboration), The XENON1T dark matter experiment, *Eur. Phys. J. C* **77**, 881 (2017).
- [11] E. Aprile *et al.* (XENON Collaboration), The neutron veto of the XENONnT experiment: Results with demineralized water (to be published).
- [12] V. C. Antochi *et al.*, Improved quality tests of R11410-21 photomultiplier tubes for the XENONnT experiment, *J. Instrum.* **16**, P08033 (2021).
- [13] E. Aprile *et al.* (XENON Collaboration), The XENONnT dark matter experiment, *Eur. Phys. J. C* **84**, 784 (2024).
- [14] E. Aprile *et al.* (XENON Collaboration), Design and performance of the field cage for the XENONnT experiment, *Eur. Phys. J. C* **84**, 138 (2024).
- [15] K. Fujii, Y. Endo, Y. Torigoe, S. Nakamura, T. Haruyama, K. Kasami, S. Mihara, K. Saito, S. Sasaki, and H. Tawara, High-accuracy measurement of the emission spectrum of liquid xenon in the vacuum ultraviolet region, *Nucl. Instrum. Methods Phys. Res., Sect. A* **795**, 293 (2015).
- [16] A. Lansiant, A. Seigneur, J. L. Moretti, and J. P. Morucci, Development research on a highly luminous condensed xenon scintillator, *Nucl. Instrum. Methods* **135**, 47 (1976).
- [17] E. Aprile *et al.* (XENON Collaboration), First indication of solar  $^8\text{B}$  neutrinos via coherent elastic neutrino-nucleus scattering with xenonnt, *Phys. Rev. Lett.* **133**, 191002 (2024).
- [18] E. Aprile *et al.* (XENON Collaboration), Double-weak decays of  $^{124}\text{Xe}$  and  $^{136}\text{Xe}$  in the XENON1T and XENONnT experiments, *Phys. Rev. C* **106**, 024328 (2022).
- [19] E. McCutchan, Nuclear data sheets for  $A = 83$ , *Nucl. Data Sheets* **125**, 201 (2015).
- [20] E. Aprile *et al.* (XENON Collaboration), Low-energy calibration of XENON1T with an internal  $^{37}\text{Ar}$  source, *Eur. Phys. J. C* **83**, 542 (2023).
- [21] M. M. Bé *et al.*, *Table of Radionuclides, Monographie BIPM-5* (Bureau International des Poids et Mesures, France, 2010), Vol. 1–5.
- [22] M. M. Bé *et al.*, *Table of Radionuclides, Monographie BIPM-5* (Bureau International des Poids et Mesures, France, 2013), Vol. 7.
- [23] E. Aprile *et al.* (XENON Collaboration), Application and modeling of an online distillation method to reduce krypton and argon in XENON1T, *Prog. Theor. Exp. Phys.* **2022**, 053H01 (2022).
- [24] E. Aprile *et al.* (XENON Collaboration), Excess electronic recoil events in XENON1T, *Phys. Rev. D* **102**, 072004 (2020).
- [25] E. Aprile *et al.* (XENON Collaboration), Radon removal in XENONnT down to the solar neutrino level (to be published).
- [26] E. Aprile *et al.* (XENON Collaboration), XENON1T dark matter data analysis: Signal reconstruction, calibration and event selection, *Phys. Rev. D* **100**, 052014 (2019).
- [27] A. Savitzky and M. J. E. Golay, Smoothing and differentiation of data by simplified least squares procedures, *Anal. Chem.* **36**, 1627 (1964).
- [28] M. Pierre, Neutrinoless double beta decay search with XENONnT, Ph.D. thesis, Ecole nationale supérieure Mines-Télécom Atlantique, 2022.
- [29] E. Aprile *et al.* (XENON Collaboration), The triggerless data acquisition system of the XENONnT experiment, *J. Instrum.* **18**, P07054 (2023).
- [30] G. Volta, Characterization and monitoring of XENONnT photosensors and search for new physics with the first XENONnT science data, Ph.D. thesis, Zurich University, 2023.
- [31] C. Wittweg, Second-order weak decays in XENON1T and future xenon time projection chambers, Ph.D. thesis, Westfälische Wilhelms-Universität Münster, 2021.
- [32] J. Aalbers *et al.* (XENON Collaboration), AxFoundation/strax: v1.2.3, [10.5281/zenodo.6620274](https://doi.org/10.5281/zenodo.6620274) (2022).
- [33] E. Aprile *et al.* (XENON Collaboration), Energy resolution and linearity of XENON1T in the MeV energy range, *Eur. Phys. J. C* **80**, 785 (2020).
- [34] J. R. Angevaere *et al.* (XENON Collaboration), XENONnT/straxen: v1.8.3, [10.5281/zenodo.6854329](https://doi.org/10.5281/zenodo.6854329) (2022).
- [35] J. R. Angevaere, First WIMP results of XENONnT and its signal reconstruction, Ph.D. thesis, Universiteit van Amsterdam, 2023.
- [36] E. Aprile *et al.* (XENON Collaboration), The XENON1T data acquisition system, *J. Instrum.* **14**, P07016 (2019).
- [37] P. Gaemers *et al.* (XENON Collaboration), XENONnT/WFSim: v1.0.2, [10.5281/zenodo.7216324](https://doi.org/10.5281/zenodo.7216324) (2022).
- [38] E. Aprile *et al.* (XENON Collaboration), Projected WIMP sensitivity of the XENONnT dark matter experiment, *J. Cosmol. Astropart. Phys.* **11** (2020) 031.
- [39] J. Allison *et al.*, Recent developments in Geant4, *Nucl. Instrum. Methods Phys. Res., Sect. A* **835**, 186 (2016).
- [40] S. Agostinelli *et al.*, Geant4—A simulation toolkit, *Nucl. Instrum. Methods Phys. Res., Sect. A* **506**, 250 (2003).
- [41] D. Ramirez *et al.* (XENON Collaboration), XENONnT/EPIX: v0.3.4, [10.5281/zenodo.7777552](https://doi.org/10.5281/zenodo.7777552) (2023).
- [42] M. Szydagis, C. Levy, G. M. Blockinger, A. Kamaha, N. Parveen, and G. R. C. Rischbieter, Investigating the XENON1T low-energy electronic recoil excess using NEST, *Phys. Rev. D* **103**, 012002 (2021).
- [43] D. Ramírez García, Simulating the XENONnT dark matter experiment: Backgrounds and WIMP sensitivity, Ph.D. thesis, Albert-Ludwigs-Universität Freiburg, 2022.
- [44] M. Abadi *et al.*, TensorFlow: Large-scale machine learning on heterogeneous systems (2015), Software available from <https://www.tensorflow.org/>.
- [45] S. Liang *et al.*, Domain-informed neural networks for interaction localization within astroparticle experiments, *Front. Artif. Intell.* **5**, 832909 (2022).

- [46] F. Jörg, D. Cichon, G. Eurin, L. Höttsch, T. M. Undagoitia, and N. Rupp, Characterization of alpha and beta interactions in liquid xenon, *Eur. Phys. J. C* **82**, 361 (2022).
- [47] F. Toschi, Design of the field cage and charge response of the XENONnT dark matter experiment, Ph.D. thesis, Albert-Ludwigs-Universität Freiburg, 2022.
- [48] M. De Deo, G. Di Carlo, W. Fulgione, A. Molinaro, S. Parlati, R. Podviianiuk, and A. Razeto, Accurate GPS-based timestamp facility for Gran Sasso National Laboratory, *J. Instrum.* **14**, P04001 (2019).
- [49] E. Aprile *et al.* (XENON Collaboration), Conceptual design and simulation of a water cherenkov muon veto for the XENON1T experiment, *J. Instrum.* **9**, P11006 (2014).
- [50] F. Pedregosa *et al.*, Scikit-learn: Machine learning in Python, *J. Mach. Learn. Res.* **12**, 2825 (2011).
- [51] E. Aprile *et al.* (XENON Collaboration), Detector signal characterization with a Bayesian network in XENONnT, *Phys. Rev. D* **108**, 012016 (2023).
- [52] P. Sorensen, Anisotropic diffusion of electrons in liquid xenon with application to improving the sensitivity of direct dark matter searches, *Nucl. Instrum. Methods Phys. Res., Sect. A* **635**, 41 (2011).
- [53] D. G. Madland *et al.*, SOURCES 4A: A Code for Calculating (alpha, n), Spontaneous Fission, and Delayed Neutron Sources and Spectra (1999), 10.2172/15215.
- [54] V. Tomasello, V. Kudryavtsev, and M. Robinson, Calculation of neutron background for underground experiments, *Nucl. Instrum. Methods Phys. Res., Sect. A* **595**, 431 (2008).
- [55] I. H. Bell, J. Wronski, S. Quoilin, and V. Lemort, Pure and pseudo-pure fluid thermophysical property evaluation and the open-source thermophysical property library coolprop, *Ind. Eng. Chem. Res.* **53**, 2498 (2014).
- [56] C. J. Clopper and E. S. Pearson, The use of confidence or fiducial limits illustrated in the case of the binomial, *Biometrika* **26**, 404 (1934).
- [57] C. E. Dahl, The physics of background discrimination in liquid xenon, and first results from XENON10 in the hunt for WIMP dark matter, Ph.D. thesis, Princeton University, 2009.
- [58] E. Aprile *et al.* (XENON Collaboration), Low-energy Neutron Calibration of XENONnT with a YBe Source (to be published).